A&A manuscript no.
(will be inserted by hand later)

Your thesaurus codes are:
02.19.1; 09.03.1; 09.09.1 Vela SNR; 09.19.1; 09.19.2; 13.21.3

ASTRONOMY AND ASTROPHYSICS
May 3, 2000

Multi-wavelength observations and modelling of shock-cloud interaction regions in the Vela Supernova Remnant

F. Bocchino[1*], **A. Maggio**[1], **S. Sciortino**[1], **and J. Raymond**[2]

[1] Osservatorio Astronomico di Palermo "G.S. Vaiana", Palazzo dei Normanni, I-90134, Palermo
[2] Harvard-Smithsonian Center for Astrophysics, Cambridge, MA 02138, USA

Received 12 November 1999; accepted 22 April 2000

Abstract. We present optical photometric and spectrophotometric observations of two selected filaments near the North rim of the Vela supernova remnant also observed in UV with the International Ultraviolet Explorer, and in X-rays with the *ROSAT* PSPC detector. From the optical data, we have derived spatially-resolved ($\sim 3''$) profiles of several emission lines across the filaments, which allowed us to resolve the post-shock region. Starting from model-independent line ratio diagnostics, we have estimated densities ($\overline{n} = 3.2 - 8.2$ cm^{-3}), temperatures ($T = 3 - 10 \times 10^4$ K), pressures ($P = 2.8 \times 10^{-10}$ dyne cm^{-2}) and ambient magnetic fields ($B = 50 - 85$ μG) in the post-shock flow. We have also found clear evidence of a relative displacement between the X-ray emission, the emission in the Hα line and the emission in the [O III] line. We have compared the measured displacement, the width of the filaments in Hα and [O III], and the peak values of selected line ratios with the predictions of a radiative shock model which describes in detail the structure of the post-shock region. Shock models with velocities around $v_s = 110$ km sec^{-1} are shown to be consistent with the optical and UV observations if we assume that the direction of propagation is tilted with respect to the line of sight. The layout of the X-ray and optical emission of the filament and their thermodynamical properties strongly suggest that the shock is travelling along increasing density gradient.

Key words: Shock waves - ISM: clouds - ISM: individual objects: Vela SNR - ISM: structure - ISM: supernova remnants - Ultraviolet: ISM

1. Introduction

Optical and UV photometric and spectrophotometric observations represent a powerful diagnostic tool for studying interstellar shocks propagating in a moderate density medium ($\geq 0.1 - 1$ cm^{-1}). Some optical and UV line ratios may be used to estimate physical quantities, such as temperature and density, independently of details of the shock models. This allows estimation of local physical conditions of the shocked plasma, which can be used for an accurate comparison with predictions based on theoretical shock models.

Recently, some studies on the small scale correlation between the optical and the X-ray emission of the Cygnus Loop have suggested the importance of the environment in shaping the optical appearance of large SNR shells. For instance, Graham et al. (1995) have analyzed Hα and [O III] images of a Cygnus Loop filament and have correlated them with the X-ray emission detected in the same regions with the *ROSAT* HRI, finding evidence of an interaction with a large ISM cloud. Levenson et al. (1998) produced a high spatial resolution atlas of the Loop in [O III], Hα and [S II], confirming that the optical emission arises only where the blast wave encounters ISM inhomogeneities.

From this point of view, the Vela SNR, unlike the Cygnus Loop, has not been systematically studied, although it has the great advantage of a small distance, recently updated to the value of 250 pc (Bocchino et al. 1999, hereafter Paper I), which is ~ 2 times nearer than the Cygnus Loop (Blair et al. 1999). Therefore the interactions of the shock with the environment can be studied in greater detail.

Osterbrock & Costero (1973) presented the first reliable measurement of the flux of some emission lines in a filament in the central region of the Vela SNR (Vela X), without spatial resolution, but with high accuracy ($\sim 10\%$ in the line ratios). The comparison of this pioneering observation with the emission model for a radiative shock by Cox (1972) yielded the first estimate of the shock velocity ($v_s \sim 140$ km/sec).

A more systematic approach of deriving the physical conditions and the metal abundances in a filament by comparing observed line ratios and the model of Dopita (1977), which predicts the ratios as a function of the physical conditions, was followed by Dopita et al. (1977). A similar approach was subsequently adopted mainly for the interpretation of optical observations of filaments in the Cygnus Loop, yielding valuable estimates of the den-

Send offprint requests to: fbocchin@estec.esa.nl
* *Present address:* ESA/ESTEC, Astrophysic Division, P.O. Box 299, 2200 AG Noordwijk, The Netherlands

sity and temperature of the shocked gas (Hester et al. 1983; Raymond et al. 1988).

Somewhat more accurate estimates of the shock velocity were obtained from measurements of C IV λ1550 and N V λ1240 line intensities for a different filament.

Based on the radiative shock model of Raymond (1979), Raymond et al. (1981) have reported shock velocities in the Vela SNR and in the Cygnus Loop between $\sim$ 85 and $\sim$ 130 km sec^{-1}, suggesting, at the same time, that resonant scattering in the UV lines could be important. The Raymond (1979) model has been revised by Cox & Raymond (1985), who also introduced the concept of "shock families", recognizable from the relative intensity of some emission lines, such as [O III] λ5007 and λ4363 Å, [O I] λ6300, and Hβ λ4686.

Other estimates of v_s in the Vela SNR filaments were given by Raymond et al. (1991) ($v_s \sim 150$ km sec^{-1}), using absorption lines from background stars, and by Jenkins & Wallerstein (1995), who detected material with a velocity of $\sim$ 100 km sec^{-1} and a density of $8.5 < n_0 < 17$ cm^{-3}, associated with the ISM accelerated by the shock wave. Most recently, Raymond et al. (1997) observed a face-on shock to avoid resonant scattering effects, and have determined that a model with $v_s = 165$ km sec^{-1} and a fraction of 30% of the total carbon locked up into grains can account for the data obtained with the Hopkins Ultraviolet Telescope (HUT). However, the lack of the N V λ1240 line casts some doubt on this interpretation.

These previous observations are affected by two limitations: first, the optical observations lack the spatial resolution needed for resolving the structure of the filament; second, until now there were few attempts to observe the same filament at optical, UV and X-ray wavelengths in order to compare physical quantities derived from different spectroscopic diagnostics and to interpret them with the same shock model.

In this work, we adopted a multi-wavelength approach for the observation and modeling of two filaments in the North of the Vela SNR shell, which we have already studied in the X-rays (Paper I). We have observed our targets both at optical and UV wavelengths, and the quantities derived from line ratios have been used for comparison with a newly computed radiative shock model, based on the early one of Raymond (1979). This has allowed us to trace the local physical conditions across the filaments with high spatial resolution, and to derive a schematic representation of the interaction between the blast wave and interstellar medium (ISM) inhomogeneities, which accounts for the observations at all wavelengths. The multi-wavelength approach to the study of middle-aged SNR is therefore of great interest for the characterization of the galactic ISM at small scales.

In Sect. 2 and 3, we will introduce our targets and the data obtained, while in Sect. 4 we will describe the analysis and the results. In Sect. 5 we discuss the results with particular emphasis on the spatial correlation between multiband observations and on the estimate of the physical conditions behind the shock. In Sect. 6 we formulate a radiative shock model which fits our data and yields an improved insight into the three-dimensional geometry of the ISM inhomogeneities. Finally, in Sect. 7 we summarize our results.

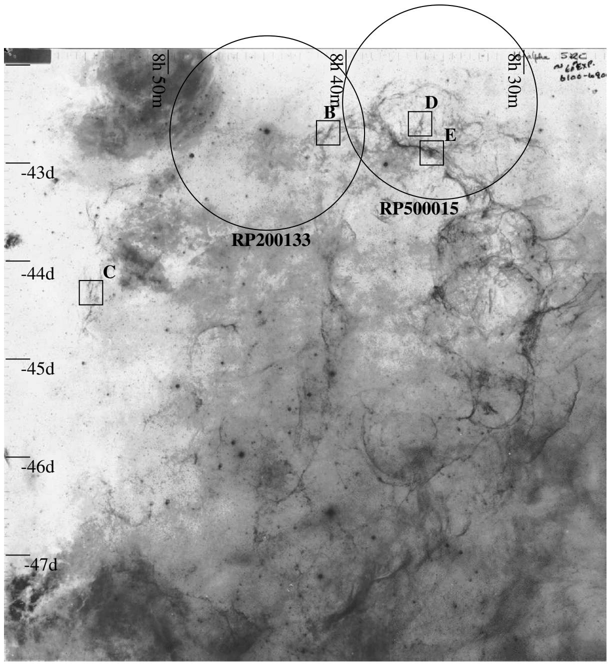

Fig. 1. Large field (5° × 5°) Schmidt plate of the Vela SNR with a red (6100-6900 Å) filter. We have superimposed the field of view of the two PSPC observation analyzed in Paper I and the positions of some filaments which we have observed in the optical.

2. Selection of the targets

The North-East region of the Vela SNR has been studied in X-rays by Bocchino et al. (1994); Bocchino et al. (1997) and in Paper I. These studies have presented strong evidence for ISM inhomogeneities interacting with the blast wave. In particular, the ISM inhomogeneities can be either in the form of isolated clouds or in the form of a cavity wall, with different implications for the X-ray morphology. For the same reason, there is great complexity of the shell appearance at optical and UV wavelengths. This is evident in Fig. 1, which shows a large field (5° × 5°) Schmidt photograph provided by John Meaburn. The image was obtained with a red filter (6100-6900 Å), and it shows mainly emission in the Hα λ6563 and the adjacent [N II] (λ6548 and λ6583) lines. In this plate, we have superimposed the 2° diameter field of view of the two *ROSAT* PSPC observations which we have analyzed in Paper I, and four squares representing the $5' \times 5'$ CCD frames taken on the filament selected for study, which we have called Filament B, C, D and E.

These filaments are somewhat prototypical regions of the optical emission of middle-aged SNRs. In particular, on the basis of the similar Hα and [O III] intensity, Filaments D and E can be classified as Type I regions, according to the classification introduced by Hester et al. (1983) (HPD hereafter), whereas Filament B includes a Type I region adjacent to a Type II region (i.e. where the [O III] emission is dominant).

In spite of the similarity of the classification, the Filaments D and E show different morphological characteristics.

A close inspection of Fig. 1 shows that Filament D (FilD) is arc-shaped and isolated. In Paper I, we have seen that this filament corresponds to a very bright X-ray region ($\sim 4' \times 1'$), whose spectral analysis revealed to be denser than the surroundings (0.9 versus 0.5 cm^{-3}). This was interpreted as evidence of interaction between the shock and an isolated ISM cloud.

Filament E (FilE), on the other hand, is part of a long network of radiative Type I filaments. The apparent size of the network (several arcminutes long), which corresponds to an X-ray front discussed in Paper I, suggested an interpretation in terms of interaction of the main shock with a cavity wall, which is common among SNR shells.

In the following, we will concentrate on Filaments D and E, while Filament B and C will be the subject of a separate work.

3. The data

3.1. Optical observations

The optical data consist of photometric and spectrophotometric CCD frames taken with ESO/MPI 2.2m telescope at La Silla (Chile) on January 20th and 21st 1996. The telescope is a f/8 Ritchey-Chretien which yields a scale of 11.7$''$/mm. The photometric images and positions of the spectrophotometer slits are shown in Fig. 2. At the telescope focus, the ESO Extended Faint Object Spectrograph and Camera (EFOSC2) allows switching between narrow band direct imaging and spectroscopy. The EFOSC2 has an efficiency of 75-80% in the 4000-10000 Å range. For the photometry, we used the following filters: Hα ESO #694, [O III] # 689, [S II] # 702. The filters, centered near the wavelengths of the corresponding emission lines, have FWHM in the range 55-65 Å. For the spectrophotometry, we used a 1$''$ slit for the science frames (a compromise between sensitivity and spectral resolution) and a 5$''$ slit for the standard stars. To cover the range between 3500 and 7000 Å, we have used grism #6 (300 lines/mm, from 4600 to 7200 Å, with a dispersion of 2.7 Å/pix, which corresponds to $\Delta\lambda = 8.1$ Å with the 1$''$ slit, and $\Delta\lambda = 40.5$ Å with the 5$''$ slit), and grism #7 (600 lines/mm, from 3580 to 4840 Å, dispersion of 1.2 Å/pix, which corresponds to $\Delta\lambda = 3.6$ Å [1$''$ slit], and $\Delta\lambda = 18$ Å [5$''$ slit]). During the observation, the efficiency of grism #7 was found to be too low, and it was only used on Filament D. Filament E was therefore observed with grism #3 (400 lines/mm, 3520-5470 Å, dispersion 1.9 Å/pix, which corresponds to $\Delta\lambda = 5.7$ and 28.5 Å with the 1$''$ and 5$''$ slit, respectively). The resolution is in any case enough to measure the line fluxes even in the worst case of the [N II] λ6548 and Hα λ6563 lines. The detector was a 1024×1024 pixel Thompson CCD (ESO # 19, 0.34$''$/pix), cooled to 149 K with liquid nitrogen, which has a read-out noise of 3.3 e$^-$ (rms), a bias of ~ 200 e^{-1}, and a dark current (measured) < 4 e$^-$ pix^{-1} hr^{-1}. The positions of the photometric and spectrophotometric frames are listed in Table 1. The seeing was 1-1.5$''$ during the observations.

Table 1. List of science frames on selected Vela SNR filaments, taken on 1996 January 20th and 21st at the 2.2m ESO/MPI telescope at La Silla (Chile). The coordinates are referred to J2000.

ID.	RA	DEC	T_{exp} (s)
Photometric frames			
Filament D	8 35 46	-42 33 02	300
Filament E	8 34 34	-42 49 35	300
Slits			
PD4	8 35 46	-42 34 35	1800
PE4	8 34 37	-42 49 35	1800

The positions of the slit (shown in Fig. 2) were chosen to sample different zones of the post-shock regions. For instance, the positions PD4 and PE4 cross perpendicular to the filament, covering regions bright either in Hα or in [O III].

3.2. UV observations

Three observations of Filament D have been carried out in the 1200-2000 Å band with the International Ultraviolet Explorer (IUE, Boggess et al. 1978), using the Short Wavelength Camera in the low-dispersion mode (spectral resolution ~ 6 Å) and Large Aperture ($10'' \times 20''$). The observations were performed on 14, 15 and 16 April 1996, and the exposure times were 400 minutes in each case. The spectra were extracted and calibrated using the IUERDAF package.

In the following we focus only on the analysis of the IUE D1 pointing, whose position is shown in Fig. 2 (top panel), because of the relatively poor signal in of the other two observations.

4. Analysis and results

4.1. Optical photometry

The narrow-band filter CCD frames were calibrated using the NOAO.IMRED package of the *Image Reduction and Analysis Facility* (IRAF). In particular, the frames have been bias subtracted, rescaled and flat-fielded using twilight flats. Flux calibration has been performed using observations of HD49798 (V=8.3, $\sim 20°$ from targets) and LTT3218 (V=11.9, $\sim 10°$ from targets), two standards included in the lists of Baldwin & Stone (1984) and Hamuy et al. (1992).

Fig. 2 shows a color composite image of Filament D (upper panel) and E (lower panel). The field of view is $5.7' \times 5.7'$ and the pixel size is $1/3''$ (the effective resolution is dominated by the seeing, $\sim 1''$). The clear distinction between [O III]-only bright filaments (shown in violet in Fig. 2) and filaments which are equally bright in [O III] and in the Low Ionization Species (LIS) group lines or brighter in the latter (shown in green) suggests that we are observing the post-shock region in great detail, and this is a novel aspect of our data with respect to previous observations.

The Hα morphology of Filament D (Fig. 2, top panel) is rather complicated. The filament is arc shaped with several clumps. The arrow labeled "EPD" indicates the expected direction of propagation of the main shock based on the position of the frame with respect of the center of the remnant.

The [O III] emission of FilD is more regular than the Hα: This characteristic has been pointed out in the Cygnus Loop (Fesen et al. 1982; Hester & Cox 1986) and seems to be related with the closeness of the [O III] emitting region to the shock front. Moreover, we note that the [O III] filament is systematically shifted toward left (west) with respect to Hα, along all the extent of the filament. This kind of shift has been noted in other SNR (e.g. in the Cygnus Loop, Hester 1987).

The corresponding color composite Hα and [O III] frame of FilE is shown in Fig. 2 (bottom panel). It is interesting to note the presence of two "fronts" in the [O III] image ("E1" and "E2"), of which only "E1" has an Hα counterpart. These filaments are less curved than Filament D, and they seem to belong to a more extended network of filaments which runs approximately in the SW-NE direction for $\sim 1°$ (see Fig. 1). This network of filaments is concave inward, which it is the opposite of the concavity expected from the interaction between a shock and an isolated cloud according to Hester (1987).

The Hα-[O III] relative shift is greater than in FilD, and is compatible with a direction of propagation from bottom to top (from South to North) in Fig. 2 (bottom panel), consistent with the expected direction of propagation of the main shock ("EPD" arrow). Finally, we note that even in the case of FilE the [O III] emission is more regular and filamentary than the Hα emission.

4.2. Optical spectrophotometry

Spectrophotometric CCD frames have been calibrated using the NOAO.SPECRED packages under IRAF. In particular the images have been bias subtracted, flat fielded using dome flats and wavelength calibrated along the dispersion direction using an HeAr lamp. The wavelength calibration is accurate at 1 Å or better over the whole bandwidth. Moreover, we have applied the following corrections: 1) atmospheric extinction using the specific La Silla coefficients, 2) cosmic ray rejection using a sigma-clipping algorithm and 3) interstellar reddening adopting $A(V) = 0.1$ (corresponding to $E(B-V) = 0.03$) on the basis of the reddening curve of Eggen (1986) for some stars in the region of the Vela SNR. In any case, the correction for interstellar reddening is very low.

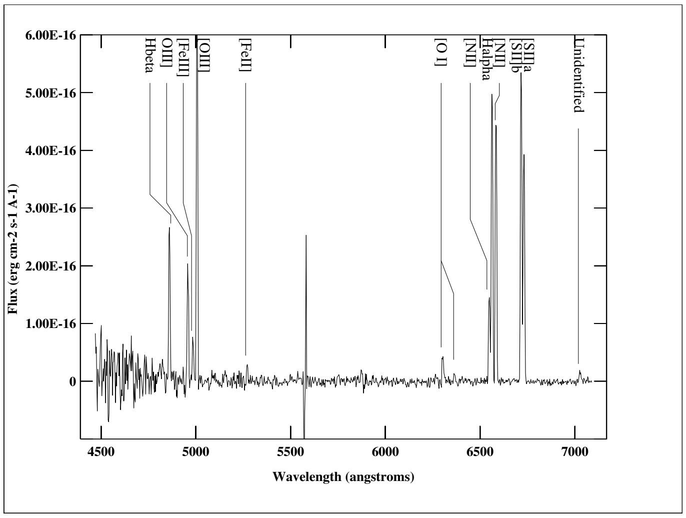

Fig. 3. Grism 6 dereddened and background subtracted spectrum at bin 40 of the PE4 slit. Some of the identified and one unidentified emission line are labelled. The spike after 5500 Å is due to the subtraction of the sky spectra.

The slit length and its position with respect to the filaments were chosen specifically to perform spatially resolved spectroscopy. For the analysis, we have chosen to group the 1024 pixels of the $5.7'$ slit along the spatial direction in 102 groups of 10 pixels each. This choice is a compromise between high spatial resolution (limited in any case by the $\sim 1.5''$ seeing) and spectra of high statistical quality. In the dispersion direction we have rebinned by a factor of 3 to match the width of the slit, and therefore our "spectroscopic" bin is 10×3 pixel (3.4×1 arcsec^2). Therefore, for each slit we have 102 bins from which we have collected 102 spectra in one shot. In Fig. 2, we show the positions of the 10th, 20th, etc. bin.

The spectra have been flux-calibrated using two spectrophotometric standards from the list of Hamuy et al. (1992), namely LTT2318 and HD49705. The background spectra have been collected in regions which show no filamentary emission in [O III] or Hα (between bin 60 and 80 in PD4, and bin 88 and 98 in PE4). We note that there is a clear diffuse emission of uncertain origin around the filaments. The background subtraction allows us to isolate the spectral features of the specific filaments we are studying.

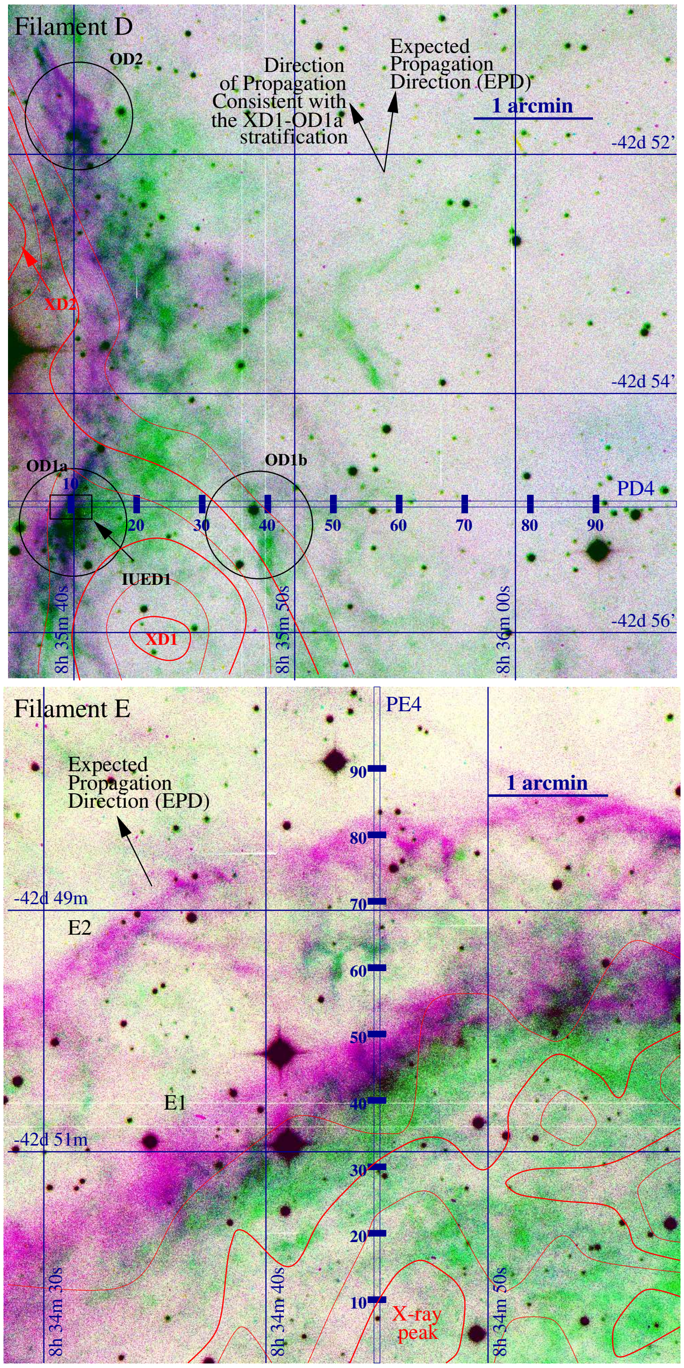

Fig. 2. Color composite CCD frames of the Filament D (*Top*) and Filament E (*Bottom*) region ($5.7' \times 5.7'$). In green, the emission in the ESO filter #694 (Hα); in violet, the emission in the ESO filter #689 ([O III] λ5007). We have superimposed the slit positions PD4 and PE4 (with numbers indicating the positions of the 10th, 20th, etc. spectral bins), the IUE pointings IUED1, the regions discussed in the text (XD1, XD2, OD1a, OD1b e OD2), the expected (EPD) and observed shock propagation directions and PSPC X-ray contours derived from the PSPC observation RP500015 (in red).

In the grism #6 spectra, we detected a total of 18 strong peaks which have been identified with known emission lines, using the list of Fesen & Hurford (1996). A few other weak peaks were detected in some of the bins, which do not have a counterpart in the list of Fesen & Hurford (1996). The unidentified peaks have not been considered for further analysis. In the spectra obtained with grisms #3 and #7, we have detected 4 additional lines, 3 of which have been identified with known emission lines. In Fig. 3, we show the spectrum of the 40th spatial bin of FilE (slit PE4) as seen by Grism #6, while in Table 2 we list all the detected lines.

Table 2. List of the detected emission lines in FilD and FilE spectra.

λ	Id.	λ	Id.
3727	[O II]	4340	Hγ
4363	[O III]	4861	Hβ
4959	O III]	4986	[Fe III]
5007	[O III]	5199	[N I]
5869	Blend HeI	5890	Na I
6300	[O I]	6364	[O I]
6435	[Ar V]	6548	[N II]
6583	[N II]	6678	[He I]
6716	[S II]	6731	[S II]

We measured the flux in the identified emission lines with an automated multi-gaussian fitting procedure, varying amplitudes, widths and centroids of the gaussian components. This procedure provides an acceptable measurement of the flux even in case of partial blending as, for instance, in the case of the [S II] lines at 6716 and 6730 Å. For each gaussian component, we rejected the best-fit result when the value of the line centroid was more distant than 2 Å from the expected value. This choice has allowed us to exclude from further analysis those bins in which the spectrum is too noisy to derive a reliable flux measurement; we have verified that, in cases of medium and high statistics, the uncertainty in the best-fit centroid is at most of 1 Å. Adopting this procedure, we have derived the flux measurements shown in Fig. 4, 5, 6 and 7, which are described in more detail in the following. The gaps in the distributions indicate noisy measurements rejected according to the screening criterion outlined above.

4.2.1. Absolute flux distributions

The flux distributions are shown in Fig. 4 for PD4 and 5 for PE4. These distributions show quantitatively that lines corresponding to different ionization potentials reach the peak emission at different locations. For instance, in the case of PD4 (Fig. 4), the peak of the emission of the [O III] line occurs at bin 7, whereas the peak of the low ionization species ([S II] and [N II], LIS group hereafter), is at bin 10. In the case of PE4 (Fig. 5), the peak of the [O III] line (bin 43) follows the peak of the LIS group (bin 40). In both cases, the relative shift is about 3 bins, corresponding to 13.2″, or 0.012 pc assuming a distance of 250 pc for the Vela SNR. In PE4, we note a second relative peak occurring around bin 61 for all the lines simultaneously. After this peak, there is a region where the [O III] line remains bright while the LIS group and the Hα lines show a decreasing emission level: we have called this region "Front E2" in Fig. 2 (bottom panel).

4.2.2. Normalized Fluxes

In order to correct the flux for the variation of the emission measure, in Fig. 6 for PD4 and Fig. 7 for PE4, we show the distributions of the line fluxes normalized to Hα = 100. In the top panels of these figures, we show the normalized Hβ/Hα ratio: since this ratio is expected to be constant, we have used the scatter around the mean value as an estimate of the uncertainty of all the other measured normalized fluxes. We have found an average Hβ/Hα ratio of 0.5 in both PD4 and PE4, with an uncertainty of 30%. We note that, since the Hβ line is less bright than the other lines (except [O I], Fig. 4 and 5), the uncertainty derived with this approach is a conservative estimate of the true uncertainties.

In both filaments, we note the presence of two kinds of regions: in the first one (corresponding to the regions labelled OD1a and OD1b in PD4, and to fronts E1 and E2 in PE4) we measure an [O III]/Hα ratio much higher than the LIS group line ratios (more than a factor of 5), while in the other case, the [O III]/Hα ratio and the LIS group line ratios are within a factor of 2.

4.2.3. Line ratios

In Fig. 8 for PD4 and Fig. 9 for PE4, we show several line ratios typically used for diagnostic purposes as a function of the coordinate along the slit. In order to further reduce the noise on these ratios, we have further screened the data rejecting pixels which have fluxes below 3×10^{-16} erg cm^{-2} s^{-1}. We show the following ratios:

[S II]/[O III] and [N II]/[O III] These ratios, which show values consistent with each other, can be used for a classification of the emitting regions. In particular, a value of $\sim$ 1 or higher identifies the "Type I" regions introduced by HPD, while a value $<$ 1 corresponds to the "Type II" regions of HPD. The top panel in Fig. 8 and 9 shows that these ratios vary by more than a factor ten along the slits. In particular, across the filaments, located between pixel 1 and 20 in PD4, and between pixel 30 and 50 in PE4 (Fig 2), they reach a minimum of $\sim$ 0.1 which is similar to the values reported by HPD on Type II filaments in the Cygnus Loop.

[O III]/[O I], [O III] (λ5007 + 4959)/4363. The [O III]/[O I] ratio is anticorrelated with the [S II]/[O III] and [N II]/[O III] ratios, indicating that, in both filaments, the local temperature of Type II regions introduced above is higher than the temperature of Type I regions. The [O III] (λ5007 + 4959)/4363 line ratio allows an estimate of the local temperature using the calibration derived by Osterbrock (1989). In both the PE4 and PD4 slits, this ratio can be reliably measured only in regions in which the [O III] is very bright. In particular, we have measured a ratio of 10-30 in the Type II regions of both PD4 (between pixel 3 and 10,

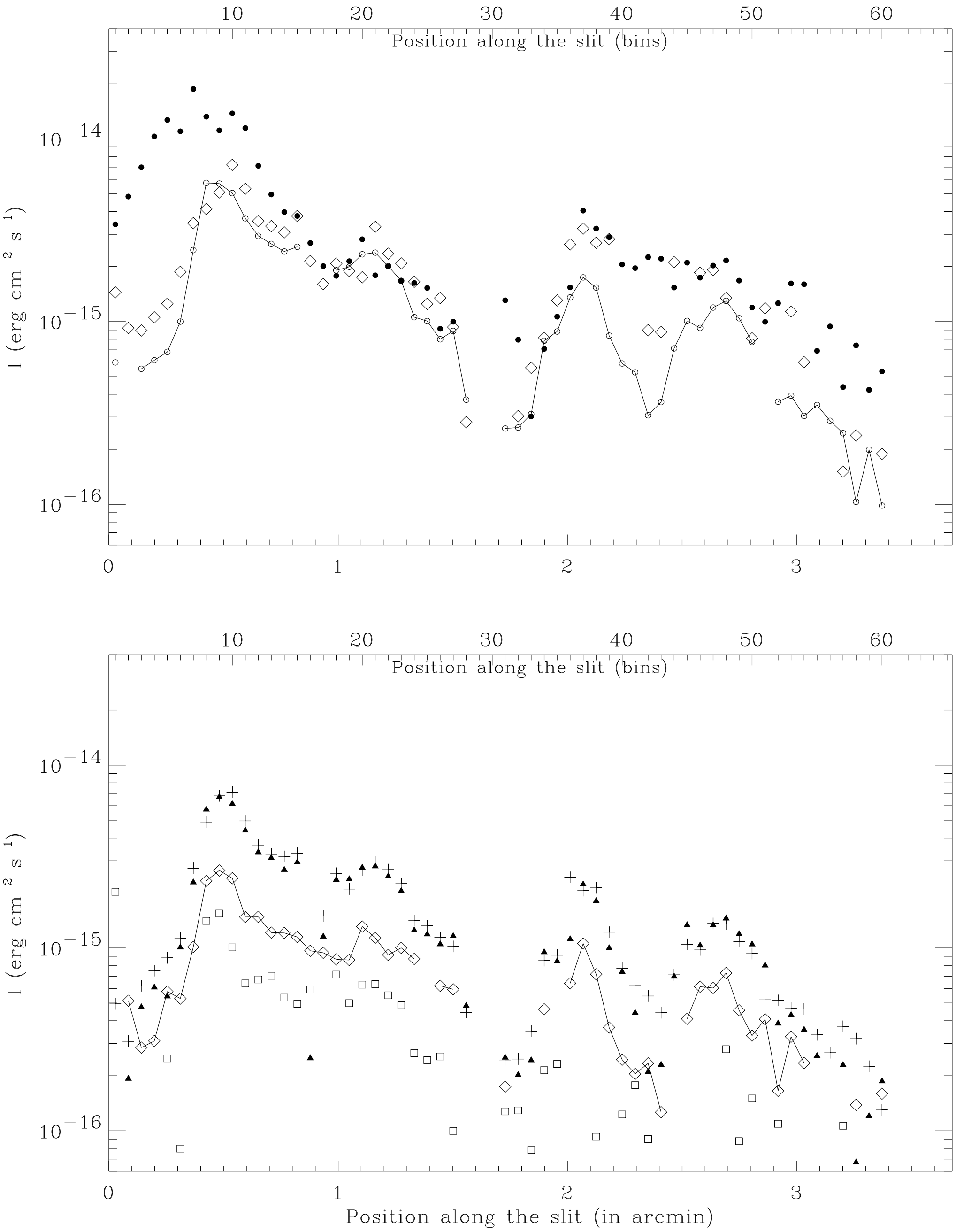

Fig. 4. Flux distributions along slit PD4. In the top panel, we show the [O III] λ5007 line (solid circles), [O II] λ3727 (open diamonds) and Hα λ6563 (open circles connected with a solid line); in the bottom panel, we show the Low Ionization Species (LIS) lines: [N II] $\lambda6548 + 6583$ (crosses), [S II] $\lambda6716 + 6730$ (filled triangles), [O I] $\lambda6300 + 6363$ (open squares), and the Hβ (open diamonds connected with a solid line). In abscissa we have the position along the slit, measured in terms of spatial bins from which the spectra have been extracted (in the top axis) and in arcminutes (bottom axis). Each spatial bin is $3.3''$ and their enumeration is also labelled in Fig. 2 to more easily locate them. The gaps in the distributions indicate measurements which are too noisy and were rejected according the screening criterion outlined in Sect. 4.2.

Fig. 8) and PE4 (between 40 and 50, Fig. 9). These values correspond to temperatures of $T \sim 3 - 10 \times 10^4$ K, according to Eq. 5.4 of Osterbrock (1989) in the low density limit.

[S II] λ6716/6730. This important line ratio is a well known density indicator, which has been calibrated by Kafatos & Lynch (1980). The observed ratios in both slits have an average value $\sim 1.3 - 1.4$:

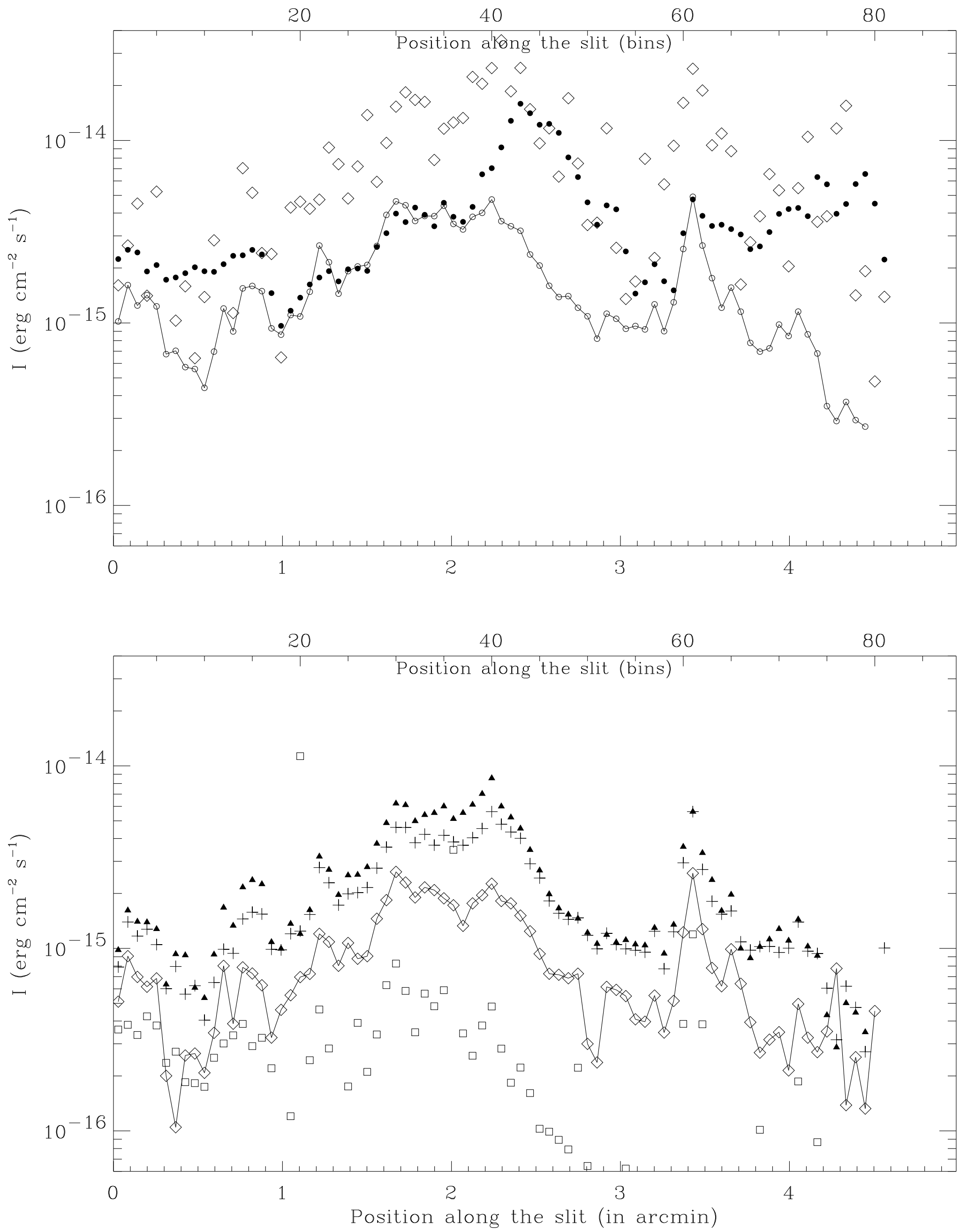

Fig. 5. Same as Fig. 4, but for PE4. The symbols are as in Fig. 4.

[N II]/Hβ, [S II]/Hβ, [O II]/Hβ. These ratios, not shown in Fig. 8 and 9, may give some clues on the abundance of nitrogen, sulphur and oxygen as suggested by Dopita (1977). However, the observed distributions are nearly constant, with values in the range 1-2, and do not fall inside the range of Dopita's calibration curves, which need to be extended for a full comparison with our data.

In summary, it is clear that regions of Type I and II coexist at angular scales of a few arcmin in those same filaments that were classified Type I only, on the basis of the large-field low-resolution plate of Fig. 1. This implies that large field observations can provide only limited results, and that a proper investigation of shock-cloud interaction requires small-scale spatially resolved data of nearby SNR shells.

4.3. UV data

In Fig. 10 we show the flux calibrated spectrum of IUE D1, integrated on the whole 10" $\times$ 20" IUE aperture. The line

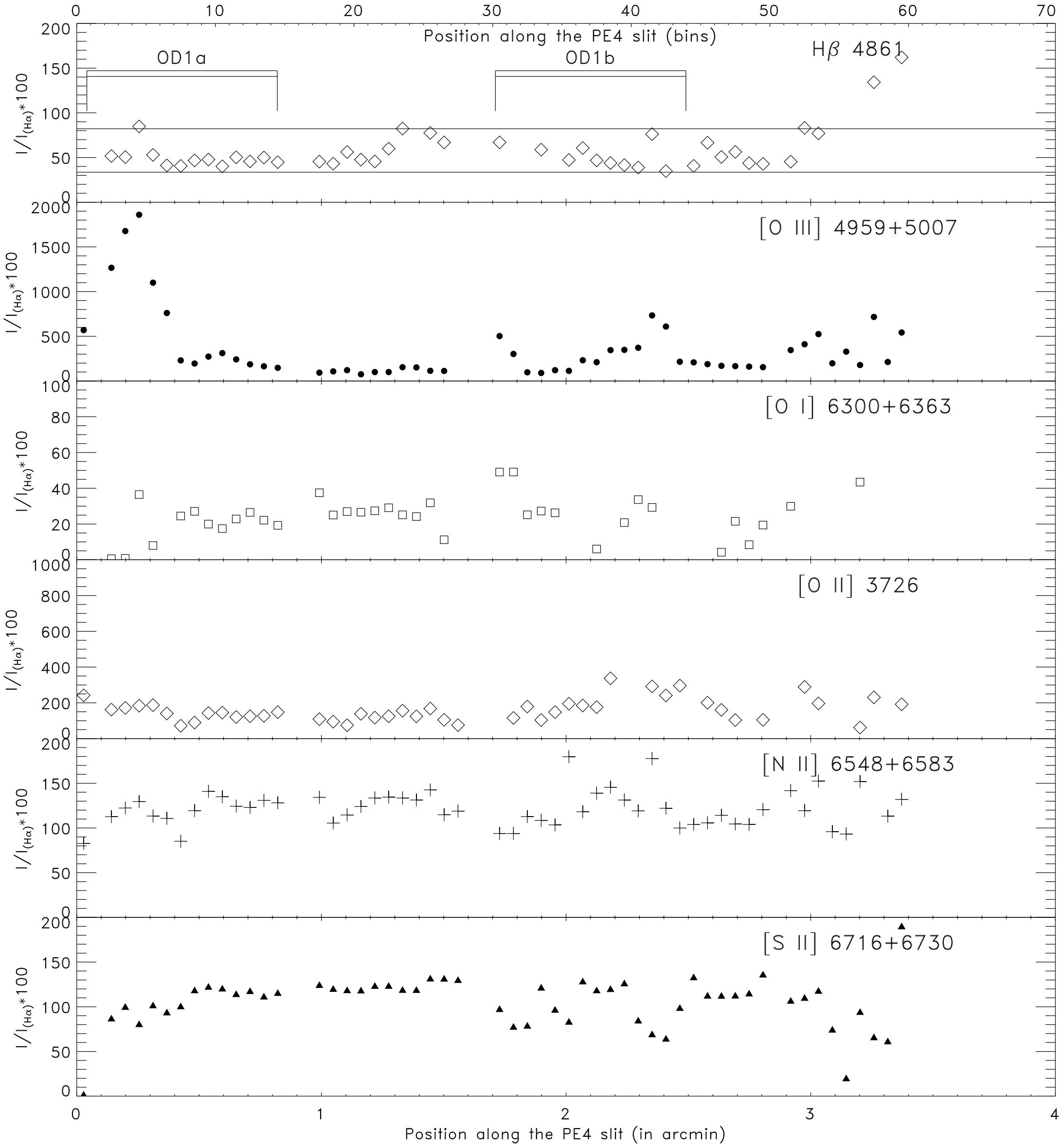

Fig. 6. Normalized flux ($I/I_{H\alpha}$) of selected emission lines along the PD4 slit. The abscissa is the same of Fig. 4 and 5.

fluxes of the detected lines, dereddened using $E(B-V) = 0.032$, have been measured by integrating the flux over a constant wavelength range of 10 Å and subtracting the nearby continuum. In Table 3, we report the results in terms of absolute flux and flux relative to H$\beta = 100$. The Hβ flux has been computed summing the flux in the 4 spatial bins of the slit PD4 which fall inside the IUE large aperture (Fig. 2, top panel), and then scaled for the ratio of the size of the optical extraction region to the size of the IUE large aperture.

Table 3. Flux of UV emission lines detected in the IUE D1 spectrum.

Line	flux (I) $\frac{10^{-13}\mathrm{erg}}{\mathrm{cm}^{-2}\mathrm{sec}^{-1}}$	I/I$_{H\beta}$ $\times100^a$	Centroid Å
N V 1240	< 0.7	< 60	undetected
SiIV+OIV] 1398+1402	1.7	150	1403.4
C IV 1548+1551	4.2	350	1548.4
He II 1640	0.7	60	1639.9
OIII] 1661+1666	2.4	200	1665.8
NIII] 1746+1749	1.3	110	1751.8
Si III] 1892+1882	2.2	190	1887.2
C III]+[CIII] 1909+1907	6.2	530	1908.1

[a] Hβ $\lambda 4861 = 1.17 \times 10^{-13}$ erg cm^{-2} sec^{-1}.

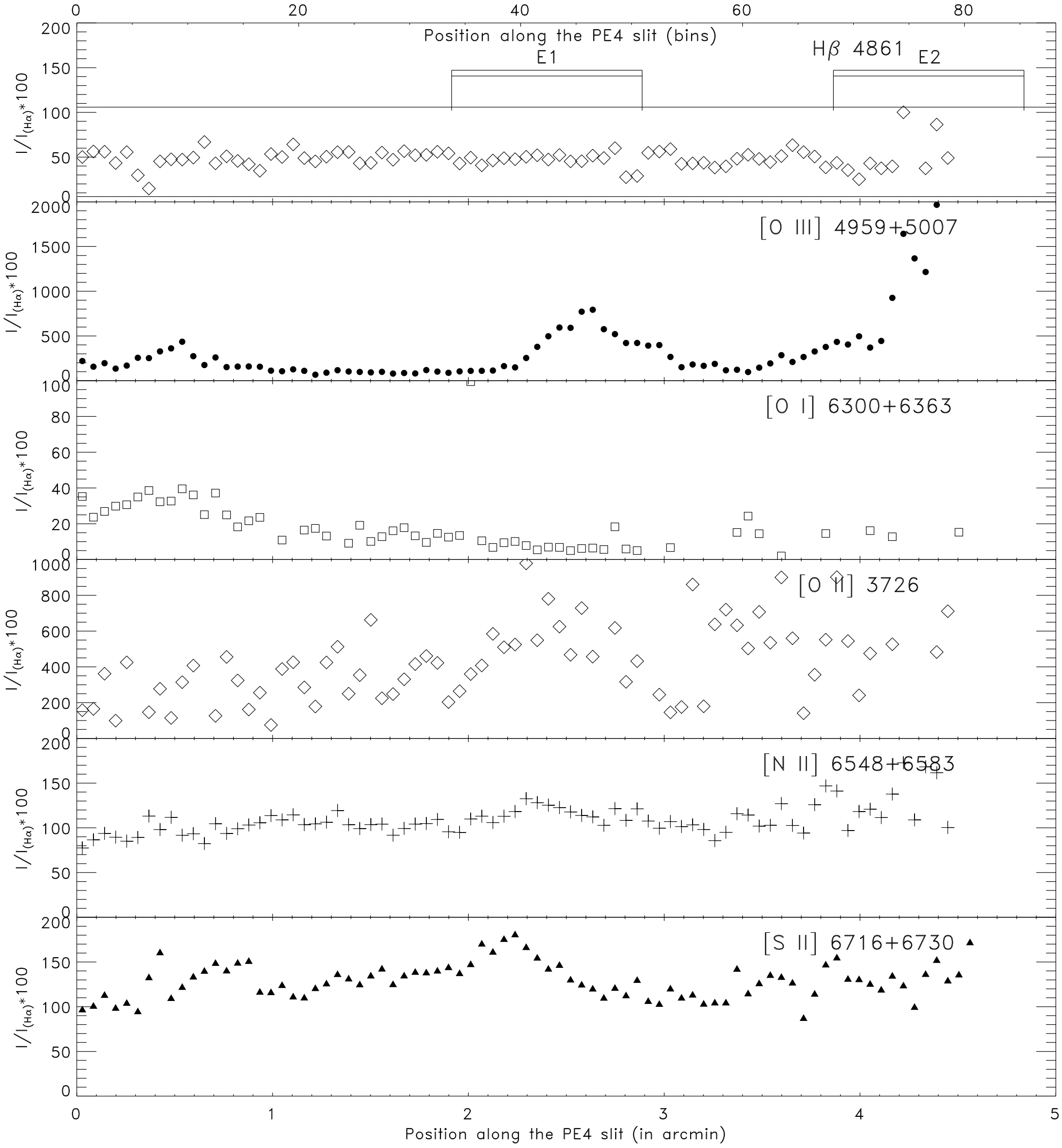

Fig. 7. Same as Fig. 6, but for the PE4 slit.

5. Discussion

5.1. Spatial correlation between optical and X-ray emission

The spatial correlation of optical and X-ray images of SNR filaments aims to understand whether the emission in these two bands shares the same origin. In Paper I we concluded that the ISM inhomogeneities play an important role in explaining the X-ray emission. In the present work, we further investigate this role by comparing the positions of the Hα and [O III] filaments with the location of the X-ray emission peak, determined from the *ROSAT* PSPC observations discussed in Paper I. This comparison, as we see below, has allowed us to measure the relative shift between the different emission regimes, which in turn has yielded to a better characterization of the medium in which expansion occurs.

Fig. 2 shows Hα-[O III] color composite images of Filament D and E, with PSPC X-ray contours superimposed. The effective PSPC spatial resolution at the position of FilD and FilE is $\sim 1'$. The expected direction of propagation of the main blast wave is indicated by the "EPD" arrows; the SNR center is therefore opposite to "EPD".

The X-ray emission of the Filament E region (Fig. 2, bottom panel) is stronger behind the optical filament E1, in a region where the Hα is weak and [O III] is absent, while it is a factor of 2 weaker (i.e. < 1.5 times stronger than the background) at Front E2. Stratification of the emission is evident along the "EPD" direction: we see, from the SNR center outward, the X-ray emission peak,

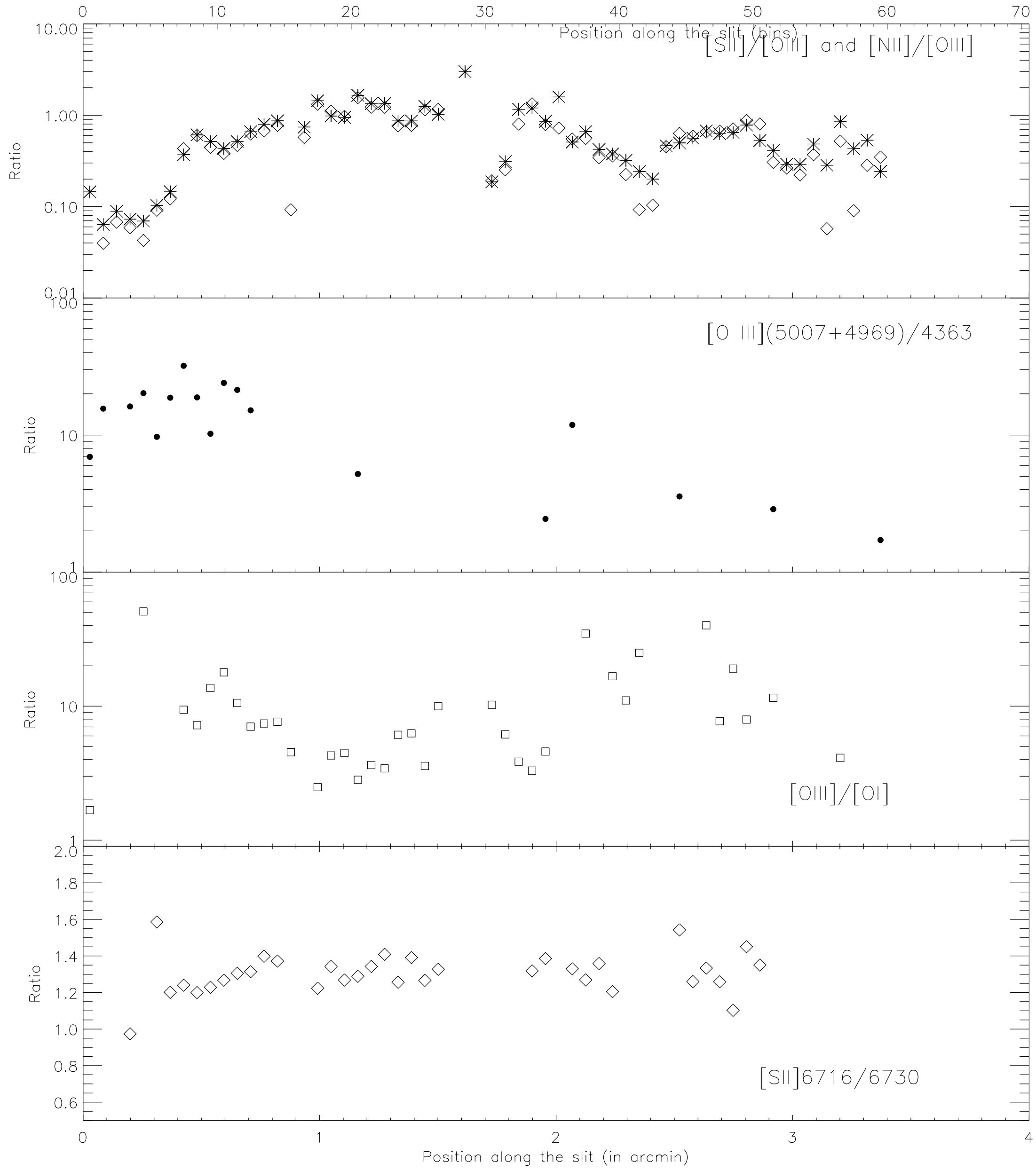

Fig. 8. Same as Fig. 6, but here we show the PD4 line ratio distributions we discuss in the text. In the top panel, [S II]/[O III] is marked with an asterisk and [N II]/[O III] with a diamond.

the $H\alpha$ and then the [O III] filament named "Front E1", a gap, and the [O III] "Front E2" filament. According to Hester (1987), stratifications such as those observed in Front E1 suggest that the shock recently encountered a high density region. The distance between the X-ray peak and Front E1 is ~ 1.5 arcmin. The relative shift between Hα and [O III] is $20 - 40$ arcsec (0.025–0.05 pc) along most of the Front E1; this is larger than analogous shifts observed in Cygnus Loop by Raymond et al. (1988) and Graham et al. (1995). The Front E2 is at 1.2–2 arcmin from E1 (0.11–0.15 pc). Its curvature is the same as that of Front E1, i.e. it is convex *outward.* A Balmer-dominated filament with the same curvature was observed in the NE of the Cygnus Loop by Hester et al. (1994), but the Cygnus filaments are much thinner (few arcseconds) than FilE ($\sim 30''$). At the resolution and sensitivity of the PSPC observation, it is not possible to study the X-ray counterpart of Front E2. Deeper and more spatially-resolved X-ray images (e.g. XMM or Chandra) will help to better correlate X-ray and optical data of this and the other regions.

The case of FilD (Fig. 2, top panel) differs from the previous case in two respects. First, the Hα emission is on the convex part of the filament, whereas the opposite occurs in FilE. This can be explained in terms of a shock propagating from right to left of Fig. 2 (top panel) and

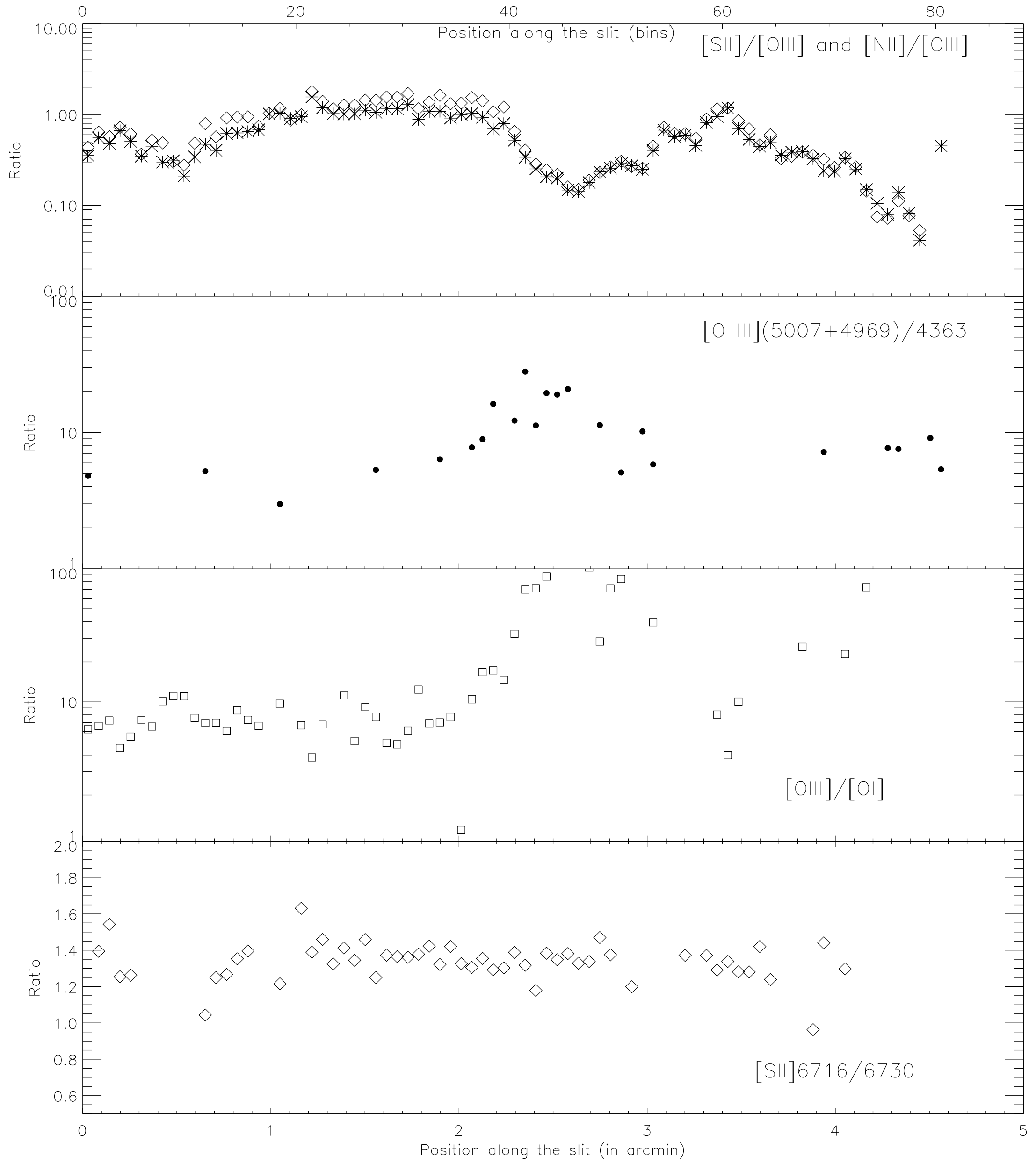

Fig. 9. Same as Fig. 7, but here we show the PE4 line ratio distributions we discuss in the text.

hitting an isolated cloud, putatively located at the extreme left. Second, the two X-ray emission peaks, XD1 and XD2, occur at the left and at the right of the optical filament, respectively. The XD1 peak position is in rough agreement with the right-to-left propagation of the shock, while the XD2 peak cannot be explained in the same way.

If the XD1 peak and the OD1a region are generated by the same shock, then the direction of the shock suggested by their alignment should be along a direction different from "EPD" as indicated in Fig. 2 (top panel). This agrees with the fact that the [O III] emission in OD1a region is on the left of the Hα region, because the [O III] bright filaments generally correspond to higher temperature zones nearer to the shock front. In an inhomogeneous environment, such as the one of the Vela SNR, it is not uncommon to find that the observed direction of propagation does not coincide with the direction of the main shock: both numerical simulations of shock-cloud interaction (e.g. Tenorio-Tagle & Rozyczka 1986) and observations of some Cygnus Loop filaments (Graham et al. 1995) show that the shock front can be distorted by the clouds and deviate from the original direction.

In and around OD2, the characterization is more complicated because regions of both Type I and Type II seem to coexist at small angular scales.

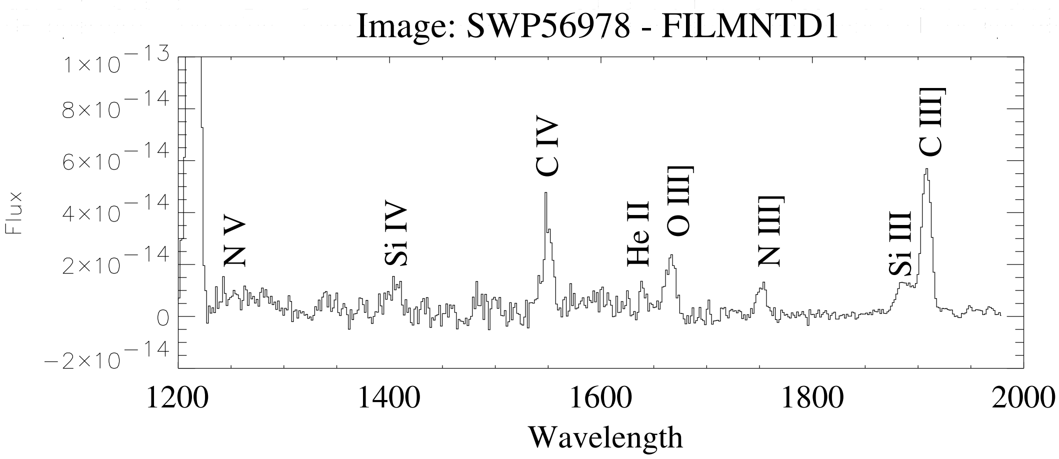

Fig. 10. IUE spectrum at the position D1. Identified lines are listed in Table 3.

5.2. Interpretation of the optical and UV emission

The "classification ratios" [S II]/Hα and [N II]/Hα have been used to distinguish between emission from a radiative shock (such as in case of SNRs) and a photo-ionized HII region. According to Levenson et al. (1995) [S II]/Hα $<$ 0.4 identifies an HII region while the opposite is true for SNRs, especially if the [N II]/Hα ratio is also > 0.3. The measured values along the slits are in agreement with a SNR shock origin.

Three different scenarios have been proposed to explain the optical and UV emission from SNR shocks: 1) the shell is in the "radiative" expansion stage; 2) there is a substantial amount of photoionization due to a fast adiabatic shock; 3) the emission is due to ISM inhomogeneities which decelerate the main blast wave. These alternative models have very different implications for the structure and nature of both the SNR and the ISM, and give different predictions of the spatial distribution of the optical and X-ray emission.

On one hand, we can safely exclude the possibility that the remnant is in its radiative phase, because substantial X-ray emission associated to the shock propagation in the ISM has been detected in Paper I. On the other hand, we can also exclude the photoionization by a fast shock as the mechanism which produces the optical emission for two reasons: first, photoionization precursors have been observed by Morse et al. (1996) and Ghavamian et al. (1999), but they are very faint and the spectrum does not look much like a shock spectrum; second, we have verified – using the X-ray derived post-shock density – that the optical emission from the post-shock region of a fast (400 km sec^{-1}) shock, as predicted according to the model of Dopita & Sutherland (1996), should occur at times larger than the Vela SNR age.

Having excluded the origin of the optical emission in terms of photoionization or SNR radiative phase, we argue that there must exist local ISM inhomogeneities with density higher than that of the X-ray emitting region (Paper I). Hence, we propose that both the optical and X-ray observations are consistently explained by postulating a density gradient in the regions where the blast wave is expanding. The situation is better clarified by Fig. 11 which shows the idealized pre-shock density profile of the ISM in this region as a function of the distance from the SNR center. The "intercloud" (IC) and "low density inhomogeneities" (LD) regions have been associated in Paper I with the high- and low-temperature X-ray components, respectively. The "high density" (HD) region, associated with the optical filaments, is approximately one order of magnitude denser than the X-ray bright regions.

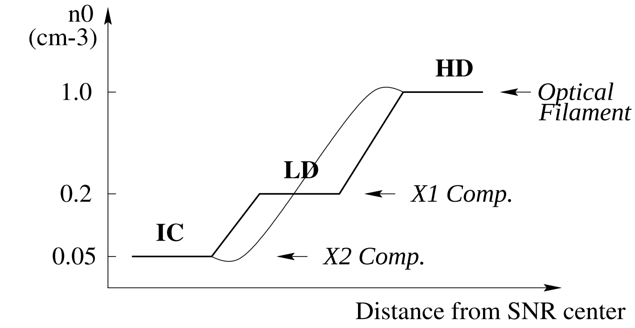

Fig. 11. Density profile consistent with X-ray and optical observations of FilD and FilE regions.

The above interpretation applies to both FilD and FilE, but the different morphology of the optical emission and the relative position of the Type I and Type II regions discussed in Sects. 4.2 and 4.3 indicates that, in case of FilD, the interaction occurs with a small ($\lesssim 1$ pc) isolated cloud which distorts the shock front, while in case of FilE, the main blast wave has encountered a large inhomogeneity, perhaps a cavity wall.

The density profile suggested in Fig. 11 is consistent with the fact that the optical filaments are external to the X-ray emission, but this stratification is not always so clear, because regions with different densities may overlap along the line of sight. This is certainly the case of the two X-ray emitting components, as suggested in Paper I, and likely also the case of the XD2 X-ray peak which appears upstream of the optical FilD. The more diffuse emission observed in FilD with respect to the more filamentary emission of FilE suggests that in the former case the viewing angle is not exactly perpendicular to the direction of propagation of the shock.

6. A radiative shock model for the high density phase

6.1. Model parameters

A radiative shock model can be characterized by four main free parameters, namely the shock velocity (v_s), the pre-shock density (n_0), the compression factor (x_m) and the pre-shock magnetic field (B_0). Starting guesses of some parameter, such as n_0 and v_s, can be obtained from the data themselves, as we will see below. Some other parameters, like the pre-shock temperature, fraction of ionized hydrogen and abundances, cannot be derived from the data, but reasonable assumptions have been made. In particular, we have assumed $T_0 = 10^4$ K, 99.9% ionized hydrogen and the following logarithmic abundances for He, C, N, O, Ne, Mg, Si, S, Ar, Ca, Fe, Ni (referred to H=12.0): 10.93, 8.32, 7.96, 8.82, 7.92, 7.52, 7.40, 7.20, 6.90, 6.30, 7.40, 6.30.

We can constrain the local density and the shock velocity using the results of the spectral analysis of the Filament D X-ray emission (Table 3 in Paper I). In fact, the ram pressure which "drives" the highly supersonic shock of the Vela SNR could be derived from the relation $P = \rho_0 v_s^2$, where ρ_0 is the pre-shock density in g cm^{-3} and v_s is the shock velocity of the X1 component which dominates the X-ray emission in the FilD region. The shock velocity is in turn computed by the best-fit X-ray temperature of X1, and it is 280 km sec^{-1} (Paper I). Since the pre-shock average plasma density is $n_0 = 0.22$ cm^{-3} (cf. with the post-shock X1 value in Table 3 of Paper I), we have $P = 2.8 \times 10^{-10}$ dyne cm^{-2}. If we assume that the optical and UV emission originates from the deceleration of the shock which has encountered a dense region, as discussed in the previous sections, then we expect that the ram pressure remains constant, as suggested by McKee & Cowie (1975). In this case, we can equate the value of P computed above with $\rho_0(UV)v_s^2(UV)$, where (UV) refers to quantities of the decelerated shock. If we assume a reasonable set of shock velocity (usually between 90 and 170 km s^{-1} for filaments in the Vela SNR), we can derive the density from the ram pressure.

The role of the magnetic field B in the SNR shell is an open problem, because it is difficult to measure and it has some influence on the extent of the post-shock region. The magnetic pressure opposes the radiative compression, and tends to enlarge the recombination region. Moreover, B also has other important effects, such as the acceleration of cosmic rays and the inhibition of thermal conduction along the direction of the field. For these reasons, it is very important to derive the magnitude of B. Here we use a classical approach to estimate B, which involves the comparison between the thermal pressure of the [S II] emitting region ($P_{[SII]} = n_{[SII]}kT_{[SII]}$) and the ram pressure of the shock. In general, the former is smaller than the latter because a fraction of the total pressure is provided by B and cosmic rays.

The doublet [S II] λ6716/6730 is a well-known model-independent density indicator in the cooling region (Dopita 1977; Kafatos & Lynch 1980). A detailed calibration of this doublet, particularly useful in the high density regime ($n \gtrsim 100$ cm^{-3}), has been provided by Blair & Kirshner (1985). We have found [S II] λ6716/6730 between 1.2 and 1.5 in PD4 and PE4, with a mean value of 1.3-1.4 (Fig. 8 and 9). Unfortunately, the observed values fall near the low-density limit of the calibration curves, and therefore we can only derive an upper limit to the density of 150 cm^{-3}. Therefore, in the [S II] emitting region, the plasma is compressed by a factor $x_1 < 50$ with respect to the density just behind the shock, and by a factor $x_0 < 200$ with respect to the ambient pre-shock density. Similar compression factors have been observed in other SNRs: for instance, Raymond et al. (1988) derived a compression factor $x_1 = 7 - 15$ for a filament in the Cygnus Loop.

From the above estimated density, we derive the thermal pressure in the cooling region. Using $n_{[SII]} < 150$ cm^{-3} and $T_{[SII]} = 8000$ K, we get $P_{[SII]} < 1.7 \times 10^{-10}$ dyne cm^{-2}, which is only 60% of the shock ram pressure we derived above. If the difference, which could be in the range $1.1 - 2.8 \times 10^{-10}$ dyne cm^{-2}, is entirely due to the magnetic pressure $P_{\rm mag} = B^2/8\pi$, then $B \sim 50 - 85\mu$G. Finally, we use the relation $x_0^2 = P_{\rm mag}/(B_0^2/8\pi)$, which links the compression factor $x_0 = n_{[SII]}/n_0$ with the pre-shock magnetic field B_0, to derive a lower limit to the ambient magnetic field ($B_0 > 0.3\mu$G.) Considering also the cosmic ray pressure in the pressure balance and if, as is often assumed, it is comparable to the magnetic pressure, we derive $B_0 > 0.2\mu$G. This low lower limit is consistent with the lack of radio counterpart of the Fil D and Fil E regions as observed by Bock et al. (1998).

6.2. Simulations

In this paragraph, we use the physical parameters estimated above to perform a number of model computations to be compared with our optical observations. This procedure provides hints on the three-dimensional layout of the shocked regions. We have used the code of Raymond (1979), updated by Butler & Raymond (1980) and Cox &

Table 4. List of the computed radiative shock models.

Num	v_s km sec^{-1}	n_0 cm^{-3}	x_m	B_0 μG
1	90	1.64	54	1.25
2	110	1.10	82	0.82
3	130	0.79	114	0.59
4	150	0.59	152	0.44

Raymond (1985). This code follows the ionization state of a parcel of plasma as it crosses the post-shock region, until it reaches a temperature of 10^3 K, and it synthesizes the fluxe of a number of lines at each point on the path, assuming that the direction of propagation is perpendicular to the line of sight. Photoionization and the photoabsorption opacities of H^0, He^0 and He^+ are included in the calculation. They become important after the gas cools to about 10,000 K and begins to recombine.

We have seen that our observations were able to resolve the post-shock flow, and therefore we have applied a full "incomplete shock model" approach, i.e. we have computed the emission distributions along the direction of the flow for a direct comparison with the data.

We have synthesized the UV lines O VI λ1034, N V λ1240, Si IV λ1398 + 1402, C IV λ1548 + 1551, O III] λ1661 + 1666, C III] λ1909, and the optical lines [O III] λ5007 + 4959, [O II] λ3727, [O I] λ6300 + 6364, [N II] λ6548 + 6584, and [S II] λ6716 + 6731. We have computed the line fluxes over a logarithmic grid of distances from the shock, ranging from 10^{14} to $\sim 10^{17}$ cm with a number of steps between 500 and 600 dynamically adapted to follow the temperature variations. The range is larger and the bin size is smaller than in previous calculations (e.g. Raymond et al. 1991) in order to match the quality of our data.

We have run the code with four choices of input parameter values, as reported in Table 4. We note that these values have been chosen so to satisfy a number of observational constraints, namely the constancy of the ram pressure ($\rho_0 v_s^2$), and the relations between the density (n_0), the compression factor ($x_m = n_{SII}/n_0$) and the pre-shock magnetic field (B_0). Model 4 is the only model which has a density and compression factor only marginally consistent with the allowed ranges.

6.3. Model results

For each simulation, we show in Fig. 12 the electron density (n_e), the ion density (n_i) and the temperature profiles as a function of distance from the shock, while the volume power density (emissivity per unit emission measure, erg cm^3 s^{-1}, times $n_e n_i$) in units of erg cm^{-3} s^{-1}, and normalized flux of the optical lines are shown in Fig. 13, 14, 15 and 16, for each computed model. For ease of comparison with the observed line distributions, the normalized fluxes have been computed integrating the line emissivity distributions times the emission measure over an extent equal to one third of the spatial bin size used in spectral analysis (i.e. 4×10^{15} cm) and dividing by the Hα flux computed in the same way. Moreover, in Fig. 17 we show the total normalized flux of the UV lines C IV, C III], O III] and N V predicted by the models vs. the shock velocity, computed by integrating the line flux distributions over the whole model range and dividing by the total Hβ flux: this allows direct comparison with the spatially-integrated IUE data.

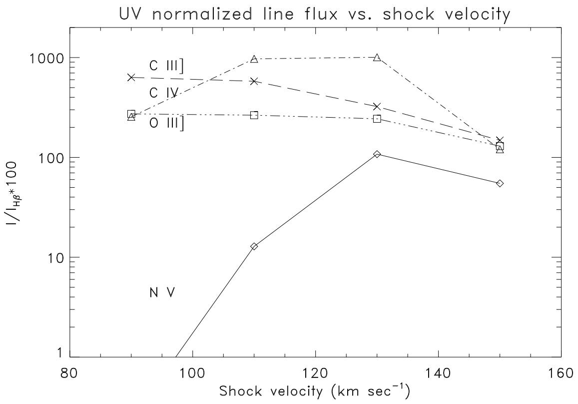

Fig. 17. Predicted normalized flux vs. shock velocity for selected UV lines

All the temperature and density profiles (Fig. 12) clearly show the onset of the radiative cooling, marked by the quick decrease of the temperature and increase of the density. At some point near $n \sim 60$ cm^{-3} and $T \sim 6 - 7 \times 10^3$ K, the heavy element recombination is so efficient that the electron density begin to decrease, while the ion density keeps increasing and the cooling rate also decreases slightly. This point separates the post-shock region into two zones: the first, nearer to the shock front, is dominated by the ionization of neutrals up to O VI, and N V and the subsequent UV radiative cooling down to O II, S II and N II; more distant from the shock, the second region is dominated by the radiation from O II, S II and N II. The O III ion forms in between these two regions. This is also suggested by the relative position of peaks in the emission distributions of the optical lines (Fig. 13-16).

Inspection of the model results shows that the optical recombination regions are not very sensitive to the input parameters. In fact, the emission distributions show that the separation between the peaks of [O III] and Hβ (or Hα) is always $< 1 \times 10^{16}$ cm, below the spatial resolution of the spectral analysis (1.2×10^{16} cm), and it does not depend on the shock velocity, whereas there is a weak dependence of the spatial width of the line peaks on the shock speed. For instance, if we consider the full width at 1/10 maximum, the widths of the LIS group peaks are between 1.5 and 2×10^{16} cm for $v_s = 90$ km sec^{-1} (Model 1), while they are between 2 and 3.5×10^{16} cm for $v_s = 150$ km sec^{-1} (Model 4); instead, the width of the Hα emission distribution is nearly constant ($\sim 3.5 \times 10^{16}$ cm).

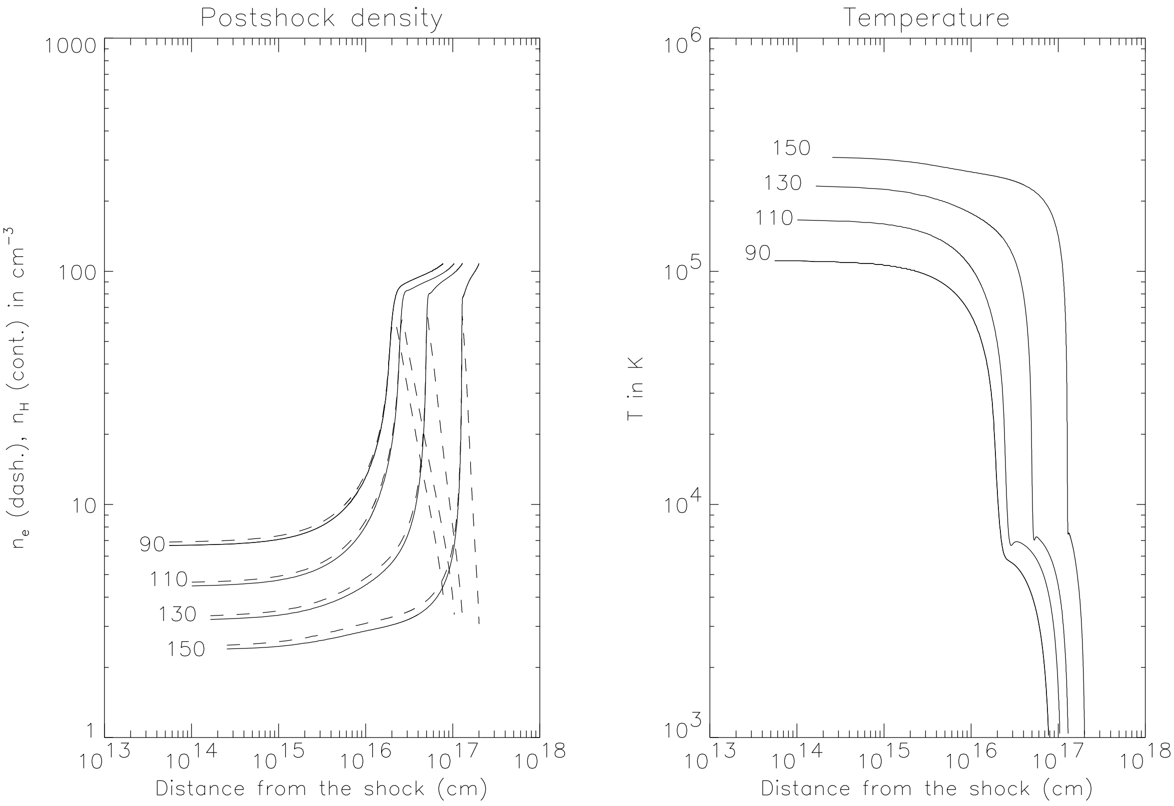

Fig. 12. Post-shock temperature and density distributions of the simulations we have performed. In the density plot, both ion (solid line) and electron (dashed line) density profiles are plotted. Numerical labels give the shock velocity in km s^{-1}.

On the other hand, Fig. 17 shows that the intensities of the UV lines are very different depending on the input shock speed. In particular, the C IV and N V lines are the best velocity indicators.

6.4. Comparison with observations

6.4.1. Shock velocity and density estimates based on UV data

We have compared the UV data with the predictions of the set of simulations we have performed (Table 4 and Fig. 17) to derive an estimate of the shock speed. We have found no N V λ1240 line in the UV spectra ($I_{\rm NV}/I_{H_\beta} * 100 < 60$) and this result yields an upper limit to the shock speed ($v_s \lesssim 120$ km sec^{-1}), as shown in Fig. 17. Moreover, the observed values of C III] $\lambda1909 + 1907$ and O III] $\lambda1661 + 1666$ ($I/I_{H_\beta} * 100 = 530$ and 200, respectively) are consistent with a shock velocity of $\lesssim 120$ and < 140 km sec^{-1}, respectively. The observed value of the C IV $\lambda1548 + 1551$ lines ($I/I_{H_\beta} * 100 = 350$) is compatible with $v_s \lesssim 100$ or $v_s \gtrsim 140$ km sec^{-1}, but we note that the C IV lines may suffer from resonant scattering along the line of sight, which would reduce the C IV intensity (Cornett et al. 1992), thus relaxing the C IV contraints on v_s.

On the other hand, the shock cannot be much slower than 80 km sec^{-1}, because in that case no optical [O III] emission would be observed for shocks with high preionization (Hartigan et al. 1987); for this reason we have not simulated a model with $v_s = 70$ km sec^{-1}. Shock velocity in the range 100-170 km sec^{-1} have been measured in other Vela SNR filaments (Raymond et al. 1981; Raymond et al. 1991, but see also Raymond et al. 1997).

Given the contraint on the ram pressure, a velocity range of 90-110 km s^{-1} corresponds to a pre-shock density in the "UV emitting" inhomogeneities in the range 0.8-2.1 cm^{-3}, 4-9 times the pre-shock density of the inhomogeneities which are responsible of the X1 X-ray emission component. Therefore, the post-shock density is in the range 3.2–8.2 cm^{-3}.

6.4.2. Comparison of flux distributions

Our models predict large variations of both the absolute fluxes and the normalized fluxes vs. the distance from the shock, and we indeed observe these variations along the slit. This implies that we are resolving the post-shock region, even though the distance from the shock cannot be easily estimated from the coordinate along the slit because of projection effects and possible inhomogeneities of the shocked medium, as explained in the following.

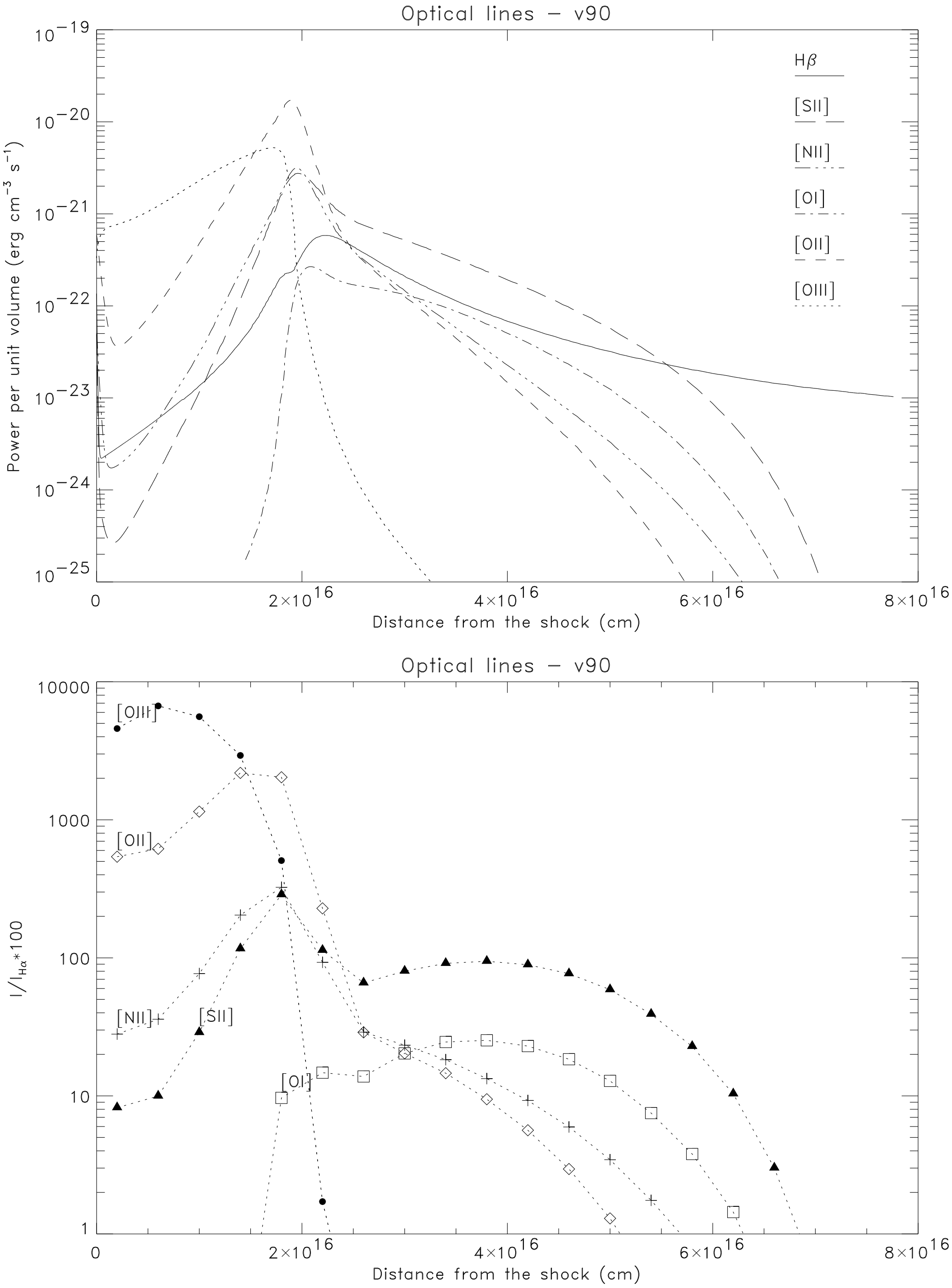

Fig. 13. Model 1. Power density (*top*) and normalized flux (*bottom*) distributions of optical lines.

For a more detailed comparison, we use 1) the predicted peak intensities and the values observed in the filaments, 2) the predicted and observed widths of the filaments, and 3) the relative separation between the [O III] emission peak and the peak of the LIS lines group.

The comparison between the model predicted peak line ratios and the values observed in the filaments (Fig. 6 and 7) is summarized in Table 5. It is noteworthy that models reproduce the data at least at a order-of-magnitude level. Moreover, the values of the ratios [N II]/Hα, [S II]/Hα and [O I]/Hα are within a factor of two of the predicted peak values, and therefore are in reasonable agreement with the model. On the other hand, the observed peak values of the [O III]/Hα are a factor of $3-4$ lower than expected and

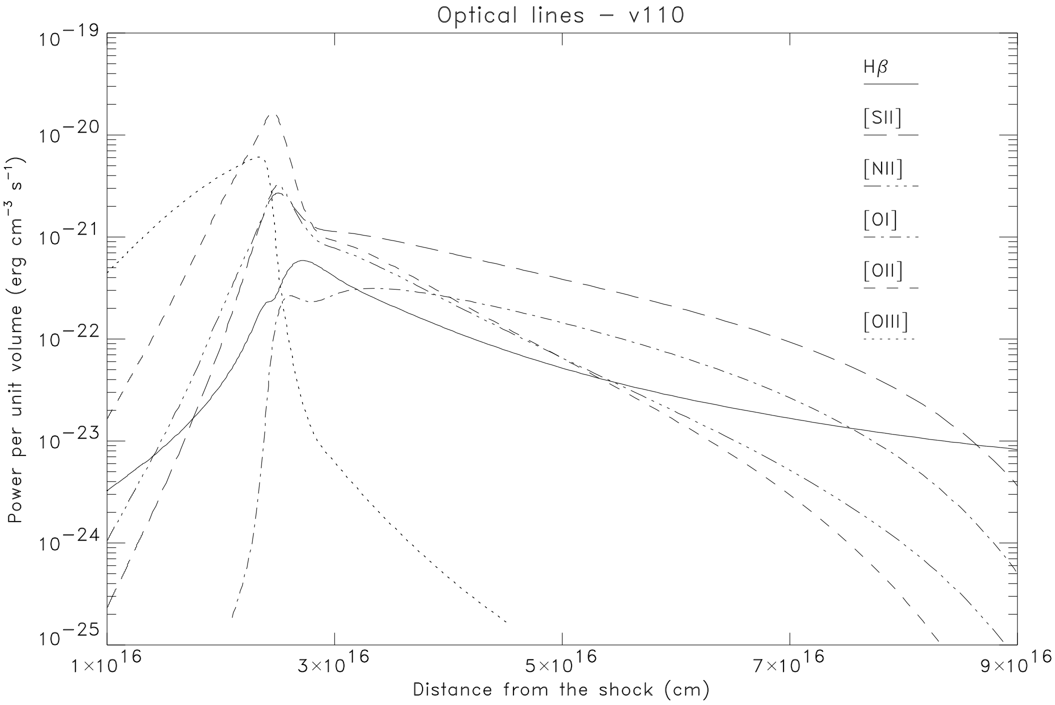

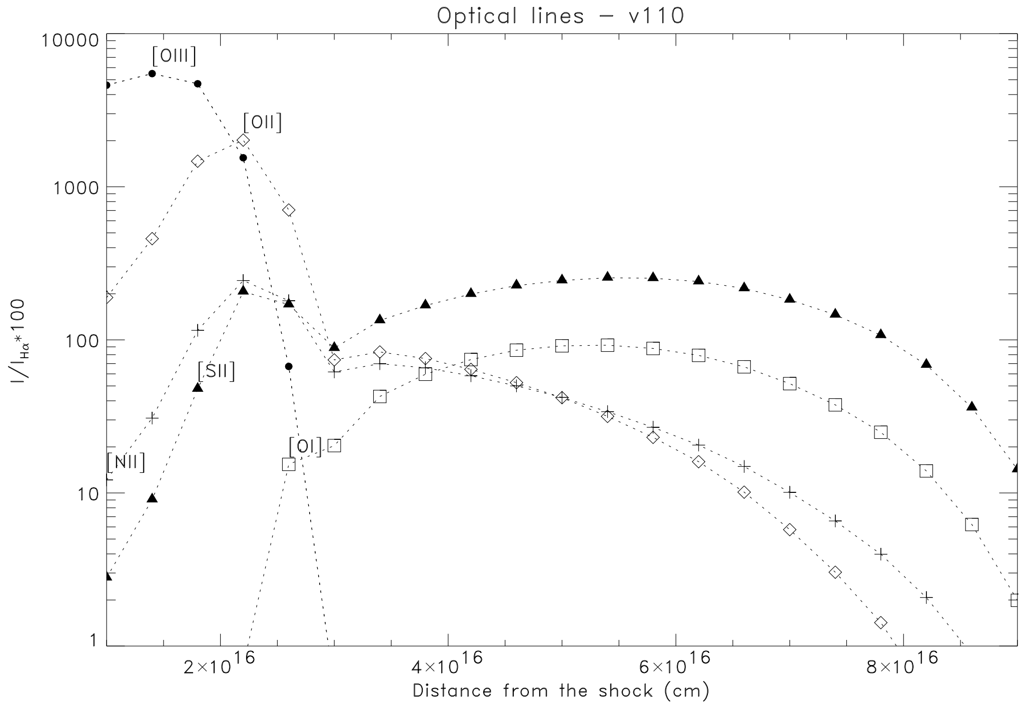

Fig. 14. Model 2. Power density (*top*) and normalized flux (*bottom*) distributions of optical lines.

the [O II]/Hα are a factor of ~ 3 lower than model predictions. The case of [O III] could be explained considering that, according to the Model 2 (Fig. 14), the peak of [O III]/Hα occurs in a region where the predicted power density of the [O III] line is a factor of 5 below its maximum value, and the Hα line power density is factor of 100 below its maximum value. Therefore, the contribution to the total filament flux coming from this region is negligible. In other words, the observed filament emission is dominated by the contribution coming from the post-shock regions where the line emissivities are near their peak values ($2-3\times10^{16}$ cm from the shock front in Model 2); here the model predicts a steep variation of the [O III]/Hα ratio from 50 down to 1, a range which brackets the observed

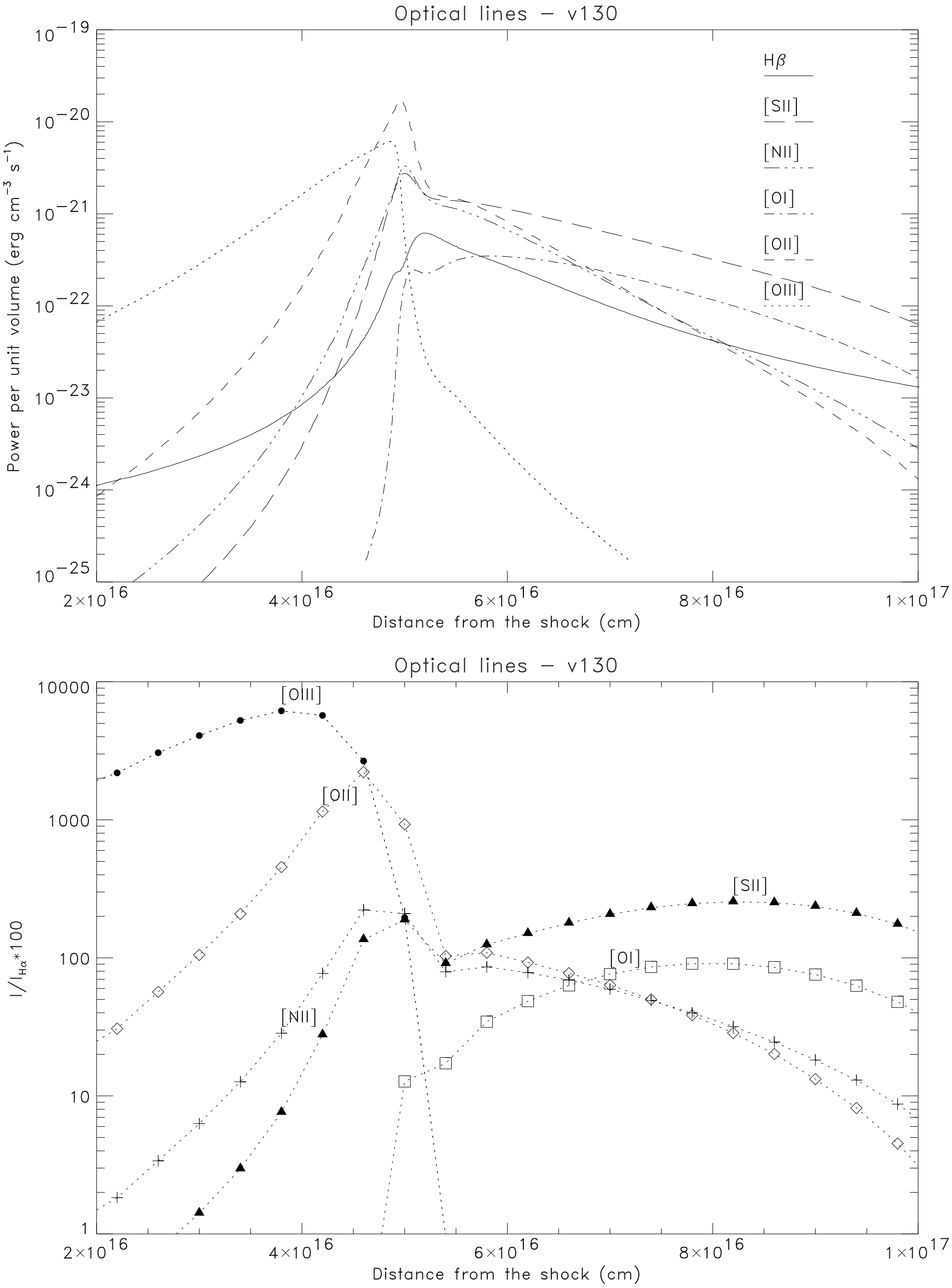

Fig. 15. Model 3. Power density (*top*) and normalized flux (*bottom*) distributions of optical lines.

ratio. The actual value of the observed ratio clearly depends on the sensitivity threshold for each line, which is difficult to estimate, because it depends on instrumental characteristics (CCD and grism efficiency vs. wavelength, exposure time, slit width). Moreover, in order to transform the flux sensitivity threshold into a power density threshold (which could be compared with the model predictions), it is necessary to compute the plasma emission measure which in turn depends on the unknown extent of the filament along the line of sight. In conclusion, the fact that we do not observe [O III]/H$\alpha \gtrsim 20$ suggests that our sensitivity is not sufficient to observe post-shock regions near the shock front where the [O III]/Hα is ~ 50 but the

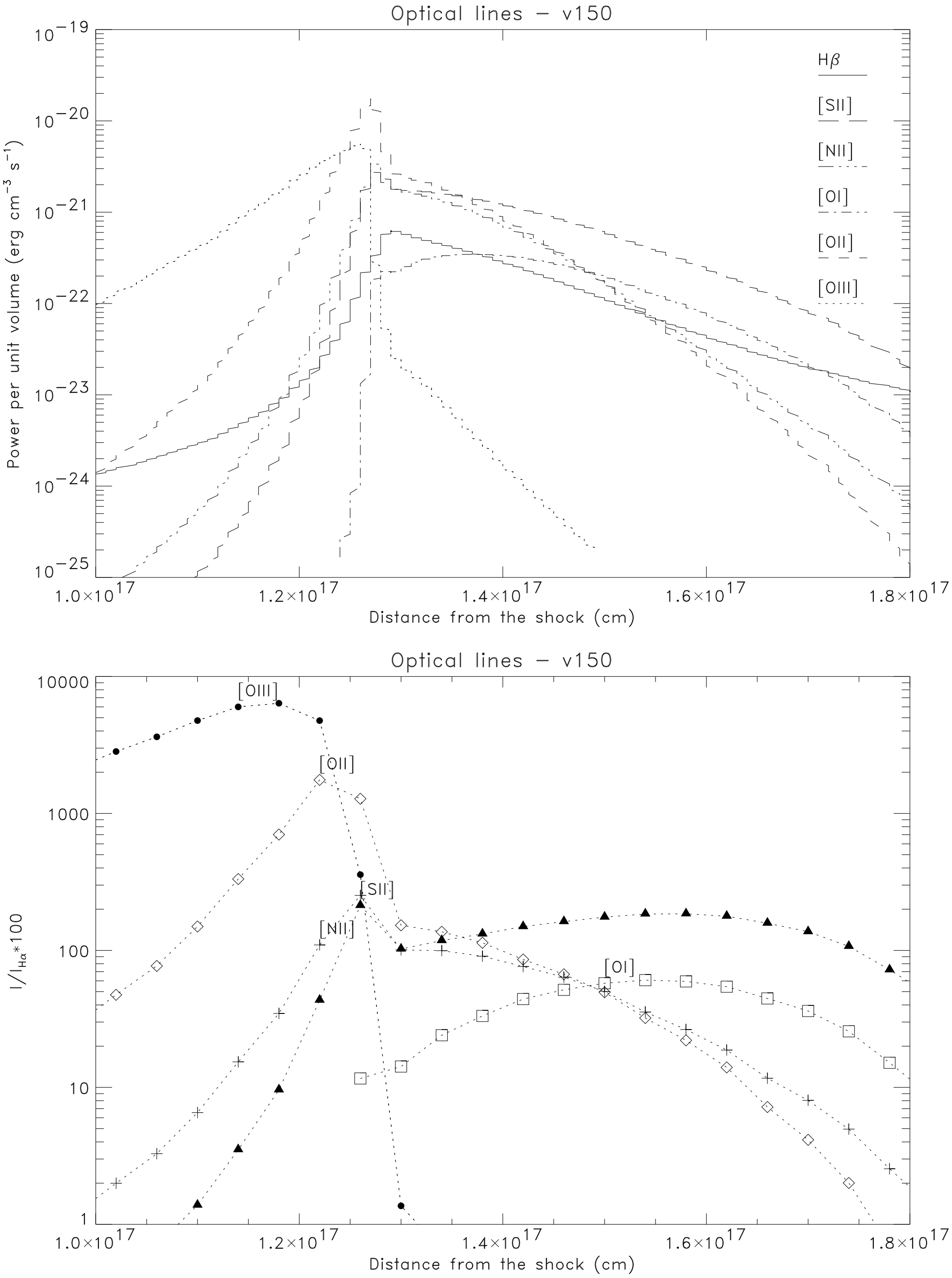

Fig. 16. Model 4. Power density (*top*) and normalized flux (*bottom*) distributions of optical lines.

line emissivities are low. The case of [O II]/Hα could also be affected by the same problem.

If the shock velocity in not exactly perpendicular to the line of sight then the line ratios are expected to be different from the values predicted by our models. In Table 5 we have reported the values predicted by the Model N of Raymond (1979), which has physical parameters similar to our Model 2, but the values are computed integrating along the whole post-shock region, a situation which corresponds to a filament seen face-on. In this case, the predicted flux of [O II], [N II], [O III] and [S II] are within a factor of two of the observation in case of PE4, while the [O I] in PE4 and [O II], [O II] and [O I] in PD4 are more

Table 5. Summary of peak predicted and observed line fluxes normalized to Hα = 100.

Line	PD4	PE4	Model 1 (peak)	Model 2 (peak)	Model 3 (peak)	Model 4 (peak)	Raymond (1979) Model N[a]
[O III] $\lambda 4959 + 5007$	1900	1000-1500	7000	5500	6000	6500	640
[O II] $\lambda 3727$	300	600-800	2500	2000	2000	1700	710
[N II] $\lambda 6548 + 6583$	150	150[b]	300	250	200	220	170
[S II] $\lambda 6716 + 6730$	140	190[b]	300	200	250	200	100
[O I] $\lambda 6300 + 6363$	20-40[b]	50	30	90	90	55	10

[a] The Raymond (1979) values differs from Model 1 because they are spatially integrated whereas Model 1 report values vs. the shock distances.
[b] No clear peak.

discrepant, indicating that the face-on model cannot fully explain the data in detail, either.

The width of the [S II] and [N II] emitting region predicted by Model 2, measured at 1/10 of the peak of the power density line distribution in Fig. 14, is $1.5 - 2 \times 10^{16}$ cm, that is 1-2 spatial bins ($3.4'' = 1.2 \times 10^{16}$ cm $= 0.004$ pc at a distance of 250 pc), and the [O III] emitting region has similar width. However, the observations show that the Hα and [O III] filaments are 3 and 5 bins FWHM wide, respectively, for PD4, and 10 and 5 bins FWHM, respectively, for PE4, while the full width at 1/10 maximum is between 15 and 20 in both slits.

The observed and predicted filament widths could be somewhat reconciled if the direction of propagation of the shock is not perpendicular to the line of sight, as also suggested by the differences between observed and predicted peaks in the flux distributions. In fact, the apparent filament width would be larger than in the ideal edge-on case, because of the sheet-like shape and optically-thin nature of the emitting regions.

On the other hand, projection effects cannot explain the large separation between the filament observed in [O III] and in other low ionization species either. In fact, if we consider the absolute flux distributions, the separation between the [O III] peak and the [N II] or [S II] peak predicted by any of the models is $< 1 \times 10^{16}$ cm $= 0.003$ pc. The width of the spatial bins of the optical spectrophotometry is $3.4'' = 1.2 \times 10^{16}$ cm $= 0.004$ pc; therefore the expected separation should be $\lesssim 1$ spatial bin, while in PE4, where the peaks are more evident, the separation is 5 bins between line ratio peaks and 2-3 bins between line flux peaks (Sect. 4.3.3 and Fig. 5 and 7). The observations therefore show a post-shock region which is more extended than predicted by our models, which assume propagation of the shock perpendicular to the line of sight. We note that even the faster shock Model 4, which has the largest recombination region, cannot explain the observed filament widths, and that projection effects would reduce the observed widths instead of increasing them.

In order to explain the discrepancy between model and observations, we argue that the shock propagates in a medium with increasing density along the direction of propagation. We have already proposed this scenario in Sect. 4.5 to explain the matching between the X-ray and the optical emission. Let us concentrate on FilE and let us assume that the configuration in this region is as shown in Fig. 18, left panel. The vertical bold lines represent isodensity contours. O is the observer and v_s is the direction of propagation of the shock. When the shock reaches the position A, it enters the Low Density (LD) region at point 1 and it decelerates down to $v_s = 300$ km sec^{-1}; the soft X-ray emission, already identified as the X1 component of Paper I, may originate in this region. After position A, the shock reaches position B and it enter the High Density (HD) inhomogeneity layer at point 2. Here the density is higher, the velocity is < 200 km sec^{-1}, and the shock becomes radiative. The spectrum at point 2 is dominated by UV and the [O III] line (Type II region of HPD). Afterwards, the shock reaches position C and enters the HD2 region at point 3. The density of HD2 cannot be lower then HD1 because otherwise we would see strong X-rays, but the observed X-ray emission is located behind the optical filaments (Fig. 2, bottom panel). At this stage, we have a "young" post-shock region in point 3 (which, however, if the HD2 density is higher than HD1, shows little [O III] emission) and in point 4, which represents the interaction of the shock at position C with the HD1 layer. At the same time, point 2 is now far from the shock front: the plasma has cooled off and the spectrum is now dominated by [N II], [O II], [S II], and the region is Type I. The observer O measures a distance i between Type II and Type I regions (that is between the peak of the [O III] and the LIS group line fluxes), whereas the corresponding distance in the model is $c = i \sin \theta$. This may explain why we observe two distinct peaks, one for [O III] and one for the LIS group lines, separated by 2-3 bins ($2.4 - 3.6 \times 10^{16}$ cm $= 0.011$ pc), which is $\sim 2-3$ times greater than the separation predicted by Model 2. The range of θ compatible with the observed separation is 20–30°. Though this low value of theta could seem improbable for a filament far from the center, we recall that if inhomogeneities have changed the local direction of the shock velocity, little could be said about the relation between theta and the distance from the SNR center.

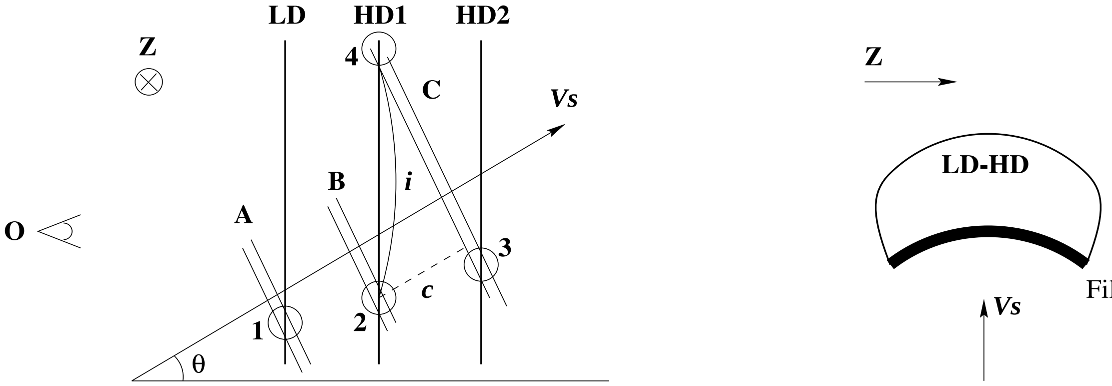

Fig. 18. *Left:* proposed stratification of ISM and its effect on the propagation of the Vela SNR shock at the position of Filament E. HD and LD are isodensity lines (that is plane-parallel inhomogeneities). For small values of θ, the angle formed by the shock speed (v_s) and the line of sight, the observer O sees the post-shock region of apparent size i. *Right:* perspective view from O which shows the shape of inhomogeneities which could reproduce the observed curvature of the Filament E.

The origin of the [O III] filament labeled "E2" in Fig. 2 (bottom panel) cannot be explained in terms of emission from the same shock which produces the "E1" front, because it is located at too large a distance from the "E1" filament. Here we are probably seeing a recent encounter of the shock with a cavity wall which is in a plane different from the one containing the cavity wall responsible for the emission in "E1".

The geometrical layout of the filament, as drawn in Fig. 18, also explains the curvature of Filament E. We have already noted that FilE is curved *inward*, whereas shock-cloud interaction are expected to produce filaments curved *outward* (Hester 1987). The observed curvature is due to the boundary of the cavity wall along the Z direction in Fig. 18. The right panel of the figure shows what is seen by the observer O, with the location of the FilE marked in bold.

In summary, the FilE region morphology is compatible with an interaction of the shock with a cavity wall created by the progenitor star. This is also in agreement with the fact that the Filament E belongs to a network of filaments which, as reported in Fig. 1, extends well beyond the boundaries of Fig. 2 (bottom panel), keeping a similar curvature. We can estimate that an element of gas which crosses a shock with $v_s = 110$ km sec^{-1} (Model 2) takes ~ 300 yr to travel 2.5×10^{16} cm (the distance between the shock front and the region where the optical lines reach their peak emission) and to produce the optical emission from low ionization species as observed in the front "E1".

Filament D has a more complex morphology than FilE, but the scheme developed for FilE can also be applied here. However, we note that the X-ray emission of Filament D is not always located on the same side of the optical filament; in particular, the XD1 peak is at the right in Fig. 2 (top panel), while the XD2 peak is at the left of the optical emission. This may imply that the local direction of propagation of the shock is not always parallel to the expected direction of propagation (arrow "EPD" in Fig. 2, top panel). This is also suggested by the stratification of optical emission layers in the OD1a region which is compatible with a new direction marked by another arrow in Fig. 2. We suggest that in OD1a the shock is entering the cloud following a different path than OD2.

The fact that we are not viewing the shock edge-on is also compatible with the presence of a diffuse background emission with spectral characteristics similar to the filaments which extends over both Filament E and D.

7. Summary and Conclusion

One of the most important results which emerges from this work is that the shock-ISM interaction is a more complex phenomenon than we previously thought. We have seen that the naive view of a purely radiative remnant dominated by optical filaments should be reviewed in terms of possibly adiabatic objects which strongly interact with ISM inhomogeneities of various shapes and sizes. The inhomogeneities can not be regarded as "small perturbations" of the remnant evolution; instead, they dramatically affect the appearance of the shell in several emission bands, even at poor spatial resolution. We stress that high spatial resolution observations in the optical and in the X-ray bands provide the key to relate the filaments, the physical processes which they represent and their ultimate origin. Since we are forced to nearby remnants to get the finer detail and these remnants are usually several degrees in size, putative interesting features of small size should be located in the shell and should be covered by high spatial resolution observations. Following this approach, we have detected two regions in the Vela shell in which there is direct evidence that the shock is propagating in a medium with a strong density gradient. In one case (Filament D), this gradient may represent an isolated cloud, whereas the other case (Filament E) is more consistent with a larger feature, perhaps a cavity wall. Comparison of photometric and spectrophotometric optical data with a radiative shock model has allowed us to derive the temperature and density in the filaments and to propose a three-dimensional model of the interaction region which is consistent with the data. In particular, we have found that $\overline{n} = 3.2 - 8.2$ cm^{-3}, $v_s \sim 90 - 110$ km sec^{-1}, $T = 3 - 10 \times 10^4$ K, $P = 2.8 \times 10^{-10}$ dyne cm^{-2} and $B = 50 - 85$ μG in the post-shock region. The shock model best describes our data if the direction of shock propagation is neither perpendicular to nor along the line of sight, but it forms an angle of 20–30°. The derived pre-shock density ($n_0 = 0.9 - 2.1$ cm^{-3}) is lower than expected for ISM clouds according the ISM model of McKee & Ostriker (1977) and updates. It is not clear if the shock will encounter regions of higher densities (the cloud cores); this seems more probable in the case of Filament D than Filament E. In any case, additional observations of selected filaments in the Vela shell will allow us to identify interactions with higher density inhomogeneities at different evolutionary stages, and therefore lead to a better comprehension of physical processes and ISM structure.

Acknowledgements. F. B., A. M. and S. S. acknowledge partial support from Ministero dell'Università e della Ricerca Scientifica (MURST) and of Agenzia Spaziale Italiana (ASI). F. B. wishes to thank Fabio Favata for his support in preparing the optical observations and analyzing the optical data.

References

Baldwin J. A., Stone R. P. S. 1984, MNRAS 206, 241
Blair W. P., Kirshner R. P. 1985, ApJ 289, 582
Blair W. P., Sankrit R., Raymond J. C., Long K. S. 1999, AJ 118, 942
Bocchino F., Maggio A., Sciortino S. 1994, ApJ 437, 209
Bocchino F., Maggio A., Sciortino S. 1997, ApJ 481, 872
Bocchino F., Maggio A., Sciortino S. 1999, A&A 342, 839
Bock D. C. J., Turtle A. J., Green A. J. 1998, AJ 116, 1886
Boggess A., Carr F. A., Evans D. C., et al. 1978, Nat 275, 372
Butler S. E., Raymond J. C. 1980, ApJ 240, 680
Cornett R. H., Jenkins E. B., Bohlin R. C., et al. 1992, ApJ 395, L9
Cox D. P. 1972, ApJ 178, 143
Cox D. P., Raymond J. C. 1985, ApJ 298, 651
Dopita M. A. 1977, ApJS 33, 437
Dopita M. A., Sutherland R. S. 1996, ApJS 102, 161
Dopita M. A., Mathewson D. S., Ford V. L. 1977, ApJ 214, 179
Eggen O. J. 1986, AJ 92, 1074
Fesen R. A., Hurford A. P. 1996, ApJS 106, 563
Fesen R. A., Blair W. P., Kirshner R. P. 1982, ApJ 262, 171
Ghavamian P., Raymond J. C., Hartigan P. 1999, ApJ submitted
Graham J. R., Levenson N. A., Hester J. J., Raymond J. C., Petre R. 1995, ApJ 444, 787
Hamuy M., Walker A. R., Suntzeff N. B., et al. 1992, PASP 104, 533
Hartigan P., Raymond J., Hartmann L. 1987, ApJ 316, 323
Hester J. J. 1987, ApJ 314, 187
Hester J. J., Cox D. P. 1986, ApJ 300, 675
Hester J. J., Parker R. A. R., Dufour R. J. 1983, ApJ 273, 219
Hester J. J., Raymond J. C., Blair W. P. 1994, ApJ 420, 721
Jenkins E. B., Wallerstein G. 1995, ApJ 440, 227
Kafatos M., Lynch J. P. 1980, ApJS 42, 611
Levenson N. A., Kirshner R. P., Blair W. P., Winkler P. F. 1995, AJ 110, 739
Levenson N. A., Graham J. R., Keller L. D., Richter M. J. 1998, ApJS 118, 541
McKee C. F., Cowie L. L. 1975, ApJ 195, 715
McKee C. F., Ostriker J. P. 1977, ApJ 218, 148
Morse J. A., Raymond J. C., Wilson A. S. 1996, PASP 108, 426
Osterbrock D. E. 1989, Astrophysics of gaseous nebulae and active galactic nuclei, Research supported by the University of California, John Simon Guggenheim Memorial Foundation, University of Minnesota, et al. Mill Valley, CA, University Science Books, 1989, 422 p.
Osterbrock D. E., Costero R. 1973, ApJ 184, L71
Raymond J. C. 1979, ApJS 39, 1
Raymond J. C., Black J. H., Dupree A. K., Hartmann L. 1981, ApJ 246, 100
Raymond J. C., Hester J. J., Cox D., Blair W. P., Fesen R. A., Gull T. R. 1988, ApJ 324, 869
Raymond J. C., Wallerstein G., Balick B. 1991, ApJ 383, 226
Raymond J. C., Blair W. P., Long K. S., et al. 1997, ApJ 482, 881
Tenorio-Tagle G., Rozyczka M. 1986, A&A 155, 120